

**EFFECT OF COOLING RATE AND COILING TEMPERATURE
ON THE FINAL MICROSTRUCTURE OF HSLA STEELS
AFTER HSM AND/OR LABORATORY TMP PROCESSING**

by

Giovanni Giuseppe Facco

B.S. in Nuclear Engineering, Pennsylvania State University, 2005

Submitted to the Graduate Faculty of
The Swanson School of Engineering in partial fulfillment
of the requirements for the degree of
Master of Science in Materials Science and Engineering

University of Pittsburgh

2009

UNIVERSITY OF PITTSBURGH
SWANSON SCHOOL OF ENGINEERING

This thesis was presented

by

Giovanni Giuseppe Facco

It was defended on

April 28, 2009

and approved by

Dr Calixto I. Garcia, Research Professor, Department of Mechanical Engineering
and Materials Science

Dr Luis E. Vallejo, Professor, Department of Civil and Environmental Engineering

Thesis Advisor: Dr Anthony J. DeArdo, William Kepler Whiteford Professor,
Department of Mechanical Engineering and Materials Science

EFFECT OF COOLING RATE AND COILING TEMPERATURE ON THE FINAL MICROSTRUCTURE OF HSLA STEELS AFTER HSM AND/OR LABORATORY TMP PROCESSING

Giovanni Giuseppe Facco, MS

University of Pittsburgh, 2009

Four different grades of High Strength Low Alloy Steels were investigated. This report presents an analysis of the effect that cooling rate and coiling temperature have on the final microstructure of these steels. First, a complete microstructural characterization of the as received hot band material was conducted with the aid of Optical Microscopy, Scanning and Transmission Electron Microscopy, and Electron Backscatter Diffraction-Image Quality analysis. Dilatometric studies to assess the transformation behavior of austenite under controlled continuous cooling conditions were conducted. The results provided the transformation temperatures for these grades. Finally the information gathered from the dilatometry was used to design a thermomechanical processing procedure where cooling rate and coiling temperature were varied and the effects studied. The results show that cooling rate has an important role in the final ferrite grain size, where in most cases samples cooled at 30 C/s to the coiling temperature showed grain refinement over those cooled at 10 C/s. The combination of the cooling rate and low coiling temperatures defined the transition from polygonal ferrite to acicular ferrite. A complete characterization of the final microstructures was carried out and the microstructural components were used to predict the yield stress value expected for a given processing condition.

TABLE OF CONTENTS

ABSTRACT.....	III
TABLE OF CONTENTS.....	IV
LIST OF TABLES.....	VI
LIST OF FIGURES.....	VIII
ACKNOWLEDGEMENTS.....	XIII
1.0 INTRODUCTION.....	1
2.0 BACKGROUND.....	2
2.1 MODERN PROCESSING OF HSLA STEELS.....	3
2.2 METALLURGY OF THE PROCESSING METHODS OF HSLA STEELS.....	4
2.2.1 Reheating/Normalizing.....	4
2.2.2 Roughing.....	6
2.2.3 Finishing.....	7
2.2.4 Cooling and Coiling.....	9
2.3 FORMATION OF FERRITE AND HIGH CARBON MICRO-CONSTITUENTS DURING TMP PROCESSING.....	11
2.4 STRENGTHENING MECHANISMS.....	13
2.4.1 Grain Size Strengthening / Hall-Petch Equation.....	14
2.4.2 Solid Solution Strengthening.....	17
2.4.3 Precipitation Strengthening.....	18
3.0 STATEMENT OF OBJECTIVES.....	23
4.0 EXPERIMENTAL PROCEDURE.....	24
4.1 MATERIALS.....	24
4.2 CONTINUOUS COOLING STUDIES.....	25
4.3 THERMOMECHANICAL PROCESSING SIMULATIONS.....	25
4.4 FINISHING ROLLING TEMPERATURE STUDY.....	28
4.5 EXPERIMENTAL TECHNIQUES AND MICROSTRUCTURAL ANALYSIS.....	29
4.5.1 Optical Microscopy.....	29
4.5.2 Scanning Electron Microscopy and EBSD-IQ.....	29
4.5.3 Transmission Electron Microscopy (TEM).....	31
4.5.4 Microhardness.....	32

5.0 RESULTS	33
5.1 HOT BAND MICROSTRUCTURAL ANALYSIS	33
5.1.1 Hot Band Analysis of 7045	34
5.1.2 Hot Band Analysis of 7038	38
5.1.3 Hot Band Analysis of 7153	42
5.1.4 Hot Band Analysis of 7631	46
5.2 TRANSFORMATION STUDY	49
5.2.1 Continuous Cooling of 7045	50
5.2.2 Continuous Cooling of 7153	52
5.2.3 Continuous Cooling of 7038	54
5.2.4 Continuous Cooling of 7631	56
5.3 THERMOMECHANICAL PROCESSING	58
5.3.1 Thermomechanical Processing of 7045	60
5.3.2 Thermomechanical Processing of 7153	63
5.3.3 Thermomechanical Processing of 7631	66
5.3.4 Thermomechanical Processing of 7038	68
6.0 DISCUSSION	73
6.1 EFFECT OF SKIN PASS IN HOT BAND MATERIAL	73
6.2 PREDICTED YIELD STRESS OF THE HOT BAND MATERIAL	74
6.3 TRANSFORMATION STUDY	76
6.4 TMP SIMULATIONS	79
7.0 CONCLUSIONS	82
BIBLIOGRAPHY	84

LIST OF TABLES

Table 1 Chemical composition of transfer bar samples received and subjected to thermomechanical processing simulations	24
Table 2 Chemical composition of hot band samples subjected to microstructural analysis and continuous cooling studies	24
Table 3 Matrix of parameters used in running TMP simulations	28
Table 4 Chemical Composition of 7045	35
Table 5 Results from the microstructural analysis of 7045 hot band materials.....	35
Table 6 Results from EBSD-IQ analysis of 7045 hot band material.....	37
Table 7 Chemical composition of 7038.....	39
Table 8 Results from the microstructural analysis of 7038 hot band materials.....	39
Table 9 Results from EBSD-IQ analysis of 7038 hot band material.....	41
Table 10 Chemical composition of 7153.....	43
Table 11 Results from the microstructural analysis of 7153 hot band materials.....	43
Table 12 Results from EBSD-IQ analysis of 7153 hot band material.....	46
Table 13 Chemical composition of 7631.....	47
Table 14 Results from the microstructural analysis of 7631 hot band materials.....	47
Table 15 Results from EBSD-IQ analysis of 7631 hot band material.....	49
Table 16 Average peak deformation stress of each alloy during compression testing. 7038 has two values for the second rolling temperature since two different conditions were used.	59
Table 17 Results from the microstructural analysis of the TMP simulation, including microhardness, for 7045	62
Table 18 Results from the microstructural analysis of the TMP simulation, including microhardness, for 7153	65
Table 19 Results of the microstructural analysis of the TMP simulation, including microhardness, for 7631	68

Table 20 Results from the microstructural analysis of the TMP simulation, including microhardness, for 7038 with a finish rolling temperature of 901 °C 71

Table 21 Results from the microstructural analysis of the TMP simulation, including microhardness, for 7038 with a finish rolling temperature of 870 °C 72

Table 22 Predicted yield stress (PYS) in MPa calculated for each hot band sample investigated 75

Table 23 Calculated yield stress predicted using extended Hall-Petch model from microstructural data analyzed from optical microscopy for 7153, 7631, and 7045 79

Table 24 Calculated yield stress predicted using extended Hall-Petch model from microstructural data analyzed from optical microscopy for 7038, “Low” denotes samples deformed at the lower finishing temperature. 80

LIST OF FIGURES

Figure 1 Showing the thermomechanical processes present in both hot-strip and plate mills from reheating to roughing to finishing and finally cooling.....	3
Figure 2 Effect of different alloying elements on austenite grain coarsening.....	5
Figure 3 Effect of deformation of austenite either above or below the austenite recrystallization temperature.....	8
Figure 4 Plot of recrystallization stop temperature vs. solute content showing the effect of many different elements used in HSLA alloys	9
Figure 5 Effect of coiling temperature on Ti microalloyed steel.....	11
Figure 6 Examples of different types of microstructures possible under different processing conditions in HSLA Steels; a, b & c) Quasipolygonal Ferrite & Bainite d) fine polygonal ferrite & pearlite e) acicular & quasipolygonal ferrite f) quasipolygonal, bainitic, & acicular ferrite	12
Figure 7 Diagram showing how many different factor contribute to the strengthening of manganese containing micro-alloyed steels.....	13
Figure 8 Illustration of dislocation pile up at the grain boundary	14
Figure 9 Effect of cooling rate on final ferrite grain size, shows conditions of both recrystallized and deformed austenite.	16
Figure 10 Effects of solid solution content on yield stress in low alloy steels	18
Figure 11 Depending on particle size, hardness, and applied stress different mechanisms provide strengthening through precipitation.	19
Figure 12 How dislocation motion through a particle shears the particle creating antiphase boundaries.	20
Figure 13 Depiction of how hard particles lead to Orowan bowing of dislocation particles. a) approach, b) sub-critical, c)critical, d)escape.....	21
Figure 14 Drawing of dilatometer sample	25
Figure 15 Schematic Drawing of Rastegaev modified compression sample for use in thermomechanical processing simulations.....	26
Figure 16 Schematic of TMP process showing approximate temperature range for each step of the process. After Tcoil, the slow cooling to room temperature is depicted as sloping curve toward the horizontal axis.	27

Figure 17 Two Kikuchi patterns showing how difference in lattice distortion can affect the image quality of the diffraction pattern (a) Ferrite, with high IQ (b) Martensite, with low IQ.....	30
Figure 18 Optical micrograph of the ferrite microstructure in 163655 csp4, prepared using 3% Nital solution.....	34
Figure 19 Secondary electron micrograph showing the microstructure in 163655 csp4 hot band material.....	36
Figure 20 High magnification Secondary electron micrograph of 163655 csp4 hot band material showing secondary phase particle (very fine carbides).....	36
Figure 21 EBSD-IQ distribution curve for 7045 Hot band material showing peaks for each phase identified	37
Figure 22 Very high magnification TEM images of 7045 hot band material, with arrows showing 2 examples of the very few well dispersed particles, shown in both bright and dark field conditions.	38
Figure 23 Optical micrograph of the ferrite microstructure in 263677 csp4, prepared using 3% Nital solution.....	39
Figure 24 Secondary electron micrograph showing the microstructure the secondary phase in the 7038 hot band material.....	40
Figure 25 EBSD-IQ distribution curve for 7038 Hot band material showing peaks for each phase identified	41
Figure 26 Very high magnification TEM images of 7038 hot band material, with arrows showing 2 examples of the very few well dispersed particles, shown in both bright and dark field conditions.	42
Figure 27 Optical micrograph of the ferrite microstructure in 272174 csp4, prepared using 3% Nital solution.....	43
Figure 28 Secondary electron micrograph showing the microstructure and secondary phase in the 7153 hot band.....	44
Figure 29 EBSD-IQ distribution curve for 7153 Hot band material showing peaks for each phase identified, 1 of 2.....	45
Figure 30 EBSD-IQ distribution curve for 7153 Hot band material showing peaks for each phase identified, 2 of 2.....	45
Figure 31 Optical micrograph of the ferrite microstructure in 272244 csp4, prepared using 3% Nital solution.....	46
Figure 32 Secondary electron SEM micrograph showing the microstructure as well as the nature of the secondary phase in the 272244 csp4 hot band material.	48

Figure 33 EBSD-IQ distribution curve for 7631 Hot band material showing peaks for each phase identified	48
Figure 34 Continuous cooling transformation diagram produced by J-Mat Pro for 7045	50
Figure 35 Optical micrographs of each cooling experiment and the as received hot band material for 7045.....	51
Figure 36 Electron micrographs of each cooling experiment and the as received hot band material for 7045.....	51
Figure 37 Continuous cooling transformation diagram produced by J-Mat Pro for 7153	52
Figure 38 Optical micrographs of each cooling experiment and the as received hot band material for 7153.....	53
Figure 39 Electron micrographs of each cooling experiment and the as received hot band material for 7153	54
Figure 40 Continuous cooling transformation diagram produced by J-Mat Pro for 7038	54
Figure 41 Optical micrographs of each cooling experiment and the as received hot band material for 7038.....	55
Figure 42 Electron micrographs of each cooling experiment and the as received hot band material for 7038	56
Figure 43 Continuous cooling transformation diagram produced by J-Mat Pro for 7631	56
Figure 44 Optical micrographs of each cooling experiment and the as received hot band material for 7631.....	57
Figure 45 Optical micrographs of each cooling experiment and the as received hot band material for 7631.....	58
Figure 46 Example flow stress plot from data taken during compression test on the MTS machine	59
Figure 47 Schematic of the processing temperatures in comparison to the transformation diagram for 7045	60
Figure 48 Microstructure resulting from TMP processing of 7045 with $T_{coil} = 650$, Left (10 c/s to coiling), Right (30 c/s to coiling).....	61
Figure 49 Microstructure resulting from TMP processing of 7045 with $T_{coil} = 600$, Left (10 c/s to coiling), Right (30 c/s to coiling).....	61
Figure 50 Microstructure resulting from TMP processing of 7045 with $T_{coil} = 550$, Left (10 c/s to coiling), Right (30 c/s to coiling).....	62
Figure 51 Schematic of the processing temperatures in comparison to the transformation diagram for 7153	63

Figure 52 Microstructure resulting from TMP processing of 7153 with $T_{coil} = 750$, Left (10 c/s to coiling), Right (30 c/s to coiling).....	64
Figure 53 Microstructure resulting from TMP processing of 7153 with $T_{coil} = 650$, Left (10 c/s to coiling), Right (30 c/s to coiling).....	64
Figure 54 Schematic of the processing temperatures in comparison to the transformation diagram for 7631	66
Figure 55 Microstructure resulting from TMP processing of 7631 with $T_{coil} = 650$, Left (10 c/s to coiling), Right (30 c/s to coiling).....	67
Figure 56 Microstructure resulting from TMP processing of 7631 with $T_{coil} = 550$, Left (10 c/s to coiling), Right (30 c/s to coiling).....	67
Figure 57 Schematic of the processing temperatures in comparison to the transformation diagram for 7153, only 1 finish rolling temperature is shows for simplicity.....	69
Figure 58 Microstructure resulting from TMP processing of 7038 with $T_{coil} = 650 @ 10 C/s$ Cooling, Left ($T_{finish} = 901$), Right ($T_{finish} = 870$).	69
Figure 59 Microstructure resulting from TMP processing of 7038 with $T_{coil} = 550 @ 10 C/s$ Cooling, Left ($T_{finish} = 901$), Right ($T_{finish} = 870$).	70
Figure 60 Microstructure resulting from TMP processing of 7038 with $T_{coil} = 650 @ 30 C/s$ Cooling, Left ($T_{finish} = 901$), Right ($T_{finish} = 870$).	70
Figure 61 Microstructure resulting from TMP processing of 7038 with $T_{coil} = 550 @ 30 C/s$ Cooling, Left ($T_{finish} = 901$), Right ($T_{finish} = 870$).	71
Figure 62 Graph showing effect of the skin pass on two samples of alloy 7038.	73
Figure 63 Chart showing the predicted yield stresses according to Hall-Petch model with dark plot points showing yield stress values measured.	75
Figure 64 Continuous Cooling Diagram showing the transformation temperatures observed in the cooling experiments for 7045.....	76
Figure 65 Continuous Cooling Diagram showing the transformation temperatures observed in the cooling experiments for 7153.....	77
Figure 66 Continuous Cooling Diagram showing the transformation temperatures observed in the cooling experiments for 7631.....	77
Figure 67 Continuous Cooling Diagram showing the transformation temperatures observed in the cooling experiments for 7038.....	78
Figure 68 Comparison plots of predicted yield stress of TMP Simulation results with hot-band analysis results	80

Figure 69 Plot of average peak stress at each deformation temperature for each alloy investigated.
..... 81

ACKNOWLEDGEMENTS

First I would like to thank my advisors, Dr. A. J. DeArdo, and Dr. C. I. Garcia. Without their guidance, knowledge and experience it would not have been possible to complete this research.

Also, I would like to thank all the other member of BAMPRI, including Dr. Hua, Dr. Cho, and R. Ordonez. Their help, during the many phases of my work, was indispensable. Dr. Goldman for all his help and words of encouragement, I thank you.

Thanks to Ternium-Siderar for funding the project as well as providing the steels used in this study.

Finally, I need to express extreme gratitude and appreciation towards my parents, friends and all of my family whom have provided all of the help, encouragement and love I needed during my studies.

1.0 INTRODUCTION

The development of High Strength Low Alloy (HSLA) steels over the past 50 years has been, and continues to be of great importance. Advances in properties like formability and weldability, and increased performance with tougher and stronger grades have allowed these high strength steels to remain competitive with other materials in performance applications like the automotive and gas and oil industries. Also, improved production and processing methods of these steels have allowed the development of more cost-effective steels for their continued use.

These advances in performance have been possible due to improved control of the final microstructure of these steels. This control is achieved through alloying advancements using solid solution and precipitation methods creating strength through dispersion and grain refinement and improved methods in the thermomechanical processing of these steels. Year after year, research leading to improvements in these areas is conducted.

As these advancements have been made, many companies have to adapt their processes in order to implement improvements. Many of these companies and that have embarked on programs to improve their current products for the transportation sector. In order to achieve this objective, a clear understanding of the fundamental microstructural characteristics of their current steels is needed. In addition, it is also important to have an understanding of the major factors in their processing that cause variation in mechanical properties. This research has been conducted in order to meet these needs and present a program for advancement in these steels.

2.0 BACKGROUND

High strength low alloy, or HSLA, steels have historically included steels with a wide variety of compositions, all with the common goal of achieving a high mechanical strength with small amounts of alloy additions.¹

As the use of HSLA steels has increased so has the knowledge of the effects and importance of alloying as well as the thermomechanical processing of these alloys. Alloying, hot-rolling, and controlled cooling all play key roles in how these steels have evolved. The alloying elements can act as solutes, or they may transform into precipitates, such as carbide or nitrides, creating barriers to dislocation and defect motion during deformation. The hot-rolling processes can affect the austenite microstructure which goes on to change the way in which the final microstructure forms. Finally, the transformation temperature and cooling rates of the steel from the austenite to ferrite regions determines how the final microstructure is formed.

Advances in the metallurgy of HSLA steels have produced some very high strength materials. But as these advances have been made, the variability of these steels, due to their dependence on processing parameters, has also become apparent. It is, therefore, of great importance to identify reproducible methods which allow for a final desired microstructure. This reproducibility has become possible through the automatic monitoring and control of the processing in all aspects from heating to deformation and finally cooling. This processing control is an engineering problem focusing on which conditions will achieve the desired properties in specific HSLA steel.

2.1 MODERN PROCESSING OF HSLA STEELS

In the modern processing of HSLA steels four processes contribute the most to the final product. Reheating, roughing, finishing and cooling all play specific roles in how these steels are engineered. Figure 1 below shows how these steps are represented in modern mills.

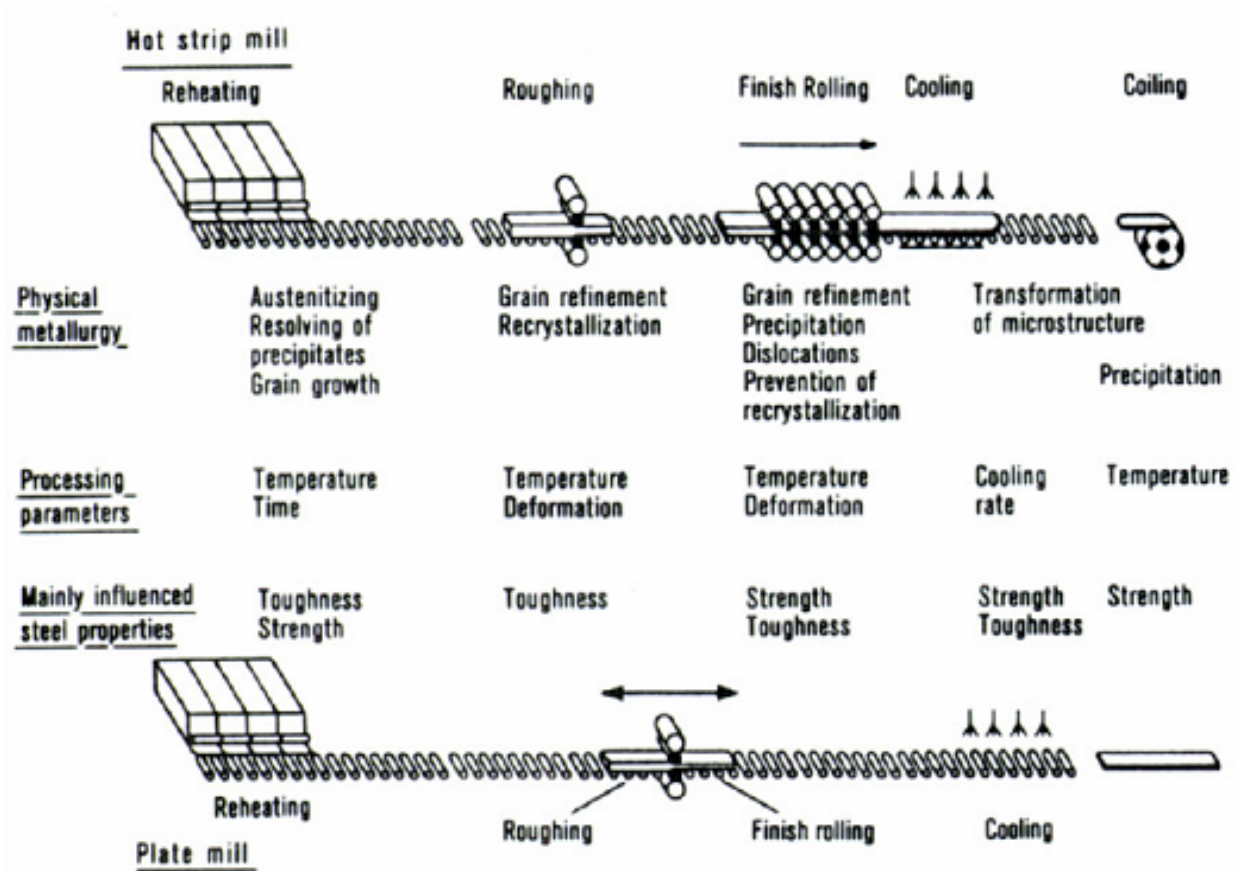


Figure 1 Showing the thermomechanical processes present in both hot-strip and plate mills from reheating to roughing to finishing and finally cooling

In the hot-strip mill process shown above, starting from the slab material the steel is first subjected to reheating. In this process, the steel is allowed to austenitize at high-temperature, allowing for some of the precipitates to dissolve and solutes to disperse. In the roughing phase, the steel is rolled for the first time, at high temperature. In this process, the large

austenite grains which had formed are deformed and then allowed to recrystallize as smaller austenite grains. Finishing refers to the final hot-rolling passes and occurs at much lower temperatures, to allow the austenite to deform but not recrystallize, this residual deformation aids in the formation of fine ferrite grain size. Finally, the steel is cooled in air or using some other cooling system, from the final rolling temperature. This cooling is rapid and continues until the steel reaches a desired coiling temperature. From there, the steel is allowed to slowly cool to ambient temperature. During this cooling, is when the nucleation of ferrite and other ambient temperature micro-constituents form, but it is through the combination of the entire thermomechanical process that determines the constitution of the final microstructure. ²

2.2 METALLURGY OF THE PROCESSING METHODS OF HSLA STEELS

2.2.1 Reheating/Normalizing

In the thermomechanical processing of HSLA products, the first step is usually reheating. In this process, the steel is brought to a high temperature and allowed to normalize. This temperature is known as the soaking or charge temperature and usually is in the range of 1150-1300 °C. This high temperature is chosen in order to allow for the dispersion of the solutes, and is also dependent upon what the precipitates present in the austenite. These precipitates, which have formed in the austenite, begin to decompose into the bulk, at high temperature, allowing the austenite grains to coarsen.³ Figure 2 shows the effect of different alloying elements on the grain size during reheating.

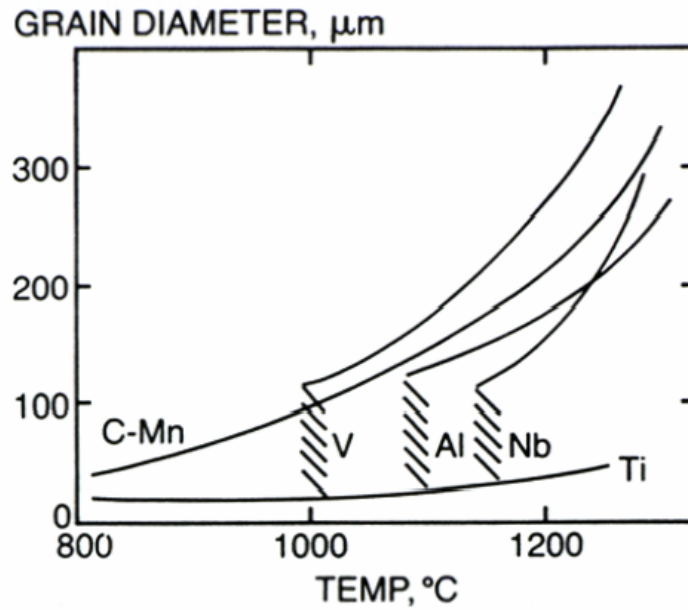


Figure 2 Effect of different alloying elements on austenite grain coarsening

In this figure the trends for vanadium, aluminum, and niobium bearing steels show grain coarsening behaviors. The temperature at which this coarsening occurs is denoted T_{gc} and is depicted by the hashing in the figure. Below the coarsening temperature, grain growth occurs in a ‘normal’ manner where grains slowly grow into each other until they are hindered by the same growth in other grains. At the grain coarsening temperature however, this growth begins to change into an abnormal or ‘secondary’ grain growth pattern. In secondary grain growth a few grains grow by consuming others then growing into the bulk of finer grains. At T_{gc} , this coarsening is just beginning to take effect and a distribution of larger ‘coarsened’ grains as well as finer grains is present. When the bulk reaches higher temperatures the secondary grains are all that remain and they continue growing normally.

The phenomenon of grain coarsening in these steels is a product of the stability and solubility of the precipitates present in the austenite grains. Below T_{gc} , these precipitates are the primary barriers to the growth of the austenite grains. Many have studied how these alloying

elements act in the steels at high temperatures. In more common grades of steel, VC and VN precipitates dissolve at lower temperatures, with other precipitates found in these HSLA steels like Nb(CN), AlN, and TiC needing temperatures in the range of 1150-1300 °C.⁴ The solubility and activity of these elements can be affected by other elements that are not participating in the precipitation itself. In the cases of Nb and C in particular the activity can be increased depending on other alloying elements decreasing the solubility of some precipitates, thereby increasing the dissolutions temperatures.

2.2.2 Roughing

After reheating, the steel is allowed to cool and move on to the roughing phase of the thermomechanical process. Roughing is where most of the plastic deformation occurs, and is intended to achieve a fine and homogeneous austenite grain structure.⁵ This grain refinement is achieved through the deformation and recrystallization of the austenite grains and means that these deforming passes must take place at temperatures usually above 1000 °C. There are many factors affecting the amount of grain refinement and, therefore, the effectiveness of the roughing pass. It has been found that the amount of deformation should be around 60% in order to achieve the maximum grain refinement for a particular roughing temperature.⁶ Also the roughing temperature itself affects the amount to which grain refinement can occur and the amount of deformation needed.

Multiple rolling passes at roughing temperatures can further refine the austenite grain size, as long as enough time is allowed to pass. This 'interpass' time, which is usually between 20-30 seconds, allows for the recrystallization to be completed before the next rolling pass

begins and deforms the grains again. Militzer et al., investigated this multipass grain refinement and developed a model to predict the effects.⁷

$$d_{rex} = Ad_0^{1/3} \varepsilon^{-P} \exp(-Q_{gx} / RT) \quad \text{for } d_{rex} < d_0 \quad (1)$$

From this equation, the final grain size (d_{rex}) can be determined from the initial grain size (d_0), the strain (ε), R as the gas constant, and other material specific parameters (Q_{gx} , A, P). Using this model, a grain refining limit is obtained. Where eventually $d_{rex} = d_0$, this limit is somewhere in the range of 20-40 μm .

2.2.3 Finishing

Like roughing, the finishing passes occur above the austenite transition temperature in order to deform the austenite grain structure. However, the finishing passes occur below the recrystallization stop temperature. This means the resulting deformed austenite grains cannot recover from the rolling fast enough and a stretched microstructure remains. Figure 3 shows the differences between deformation above and below the recrystallization stop temperature, T_{RXN} .

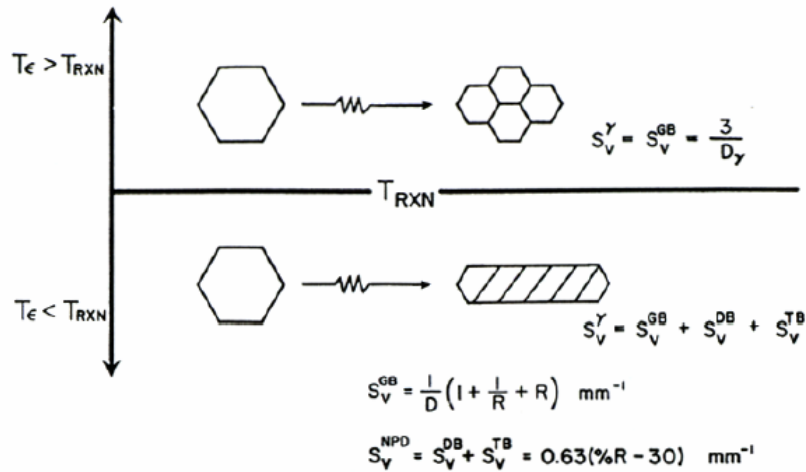


Figure 3 Effect of deformation of austenite either above or below the austenite recrystallization temperature.

The elongated and deformed grains produced in the finishing passes create nucleation sites for the formation of a fine grained ferrite structure later on in the TMP process. Generally, the recrystallization stop temperature can be defined as the temperature at which the structure has not fully recrystallized 15 seconds after a particular process.⁸

This controlled rolling resulting in a deformed austenite matrix is vital to achieving a fine ferrite grain structure. Without this un-recrystallized structure, HSLA type steels would tend to transform into bainitic structures, resulting in a less desirable product with reduced toughness.⁹ Figure 3 also shows equations for S_V , a parameter which is a quantification of the amount of defects present in the austenite matrix ,like grain boundaries, twin boundaries, deformation banding, etc,. These defects correlate to ferrite nucleation sites and, therefore, S_V has a strong relation to the final ferrite grain size.

Finally, the alloying elements present in the steel can affect the recrystallization process by changing the recrystallization stop temperature and pinning the movement of crystalline defects. For example, the additions of niobium and titanium tend to result in the formation of

carbonitride precipitates at the grain boundaries, pinning them in place. Effects such as solute drag by segregation to the grain boundaries are also important factors.¹⁰ Figure 4 shows how the different alloying elements can affect the recrystallization stop temperature. Each element affects T_{rxn} differently, exemplifying how each of them suppresses recrystallization in differing amounts.¹¹

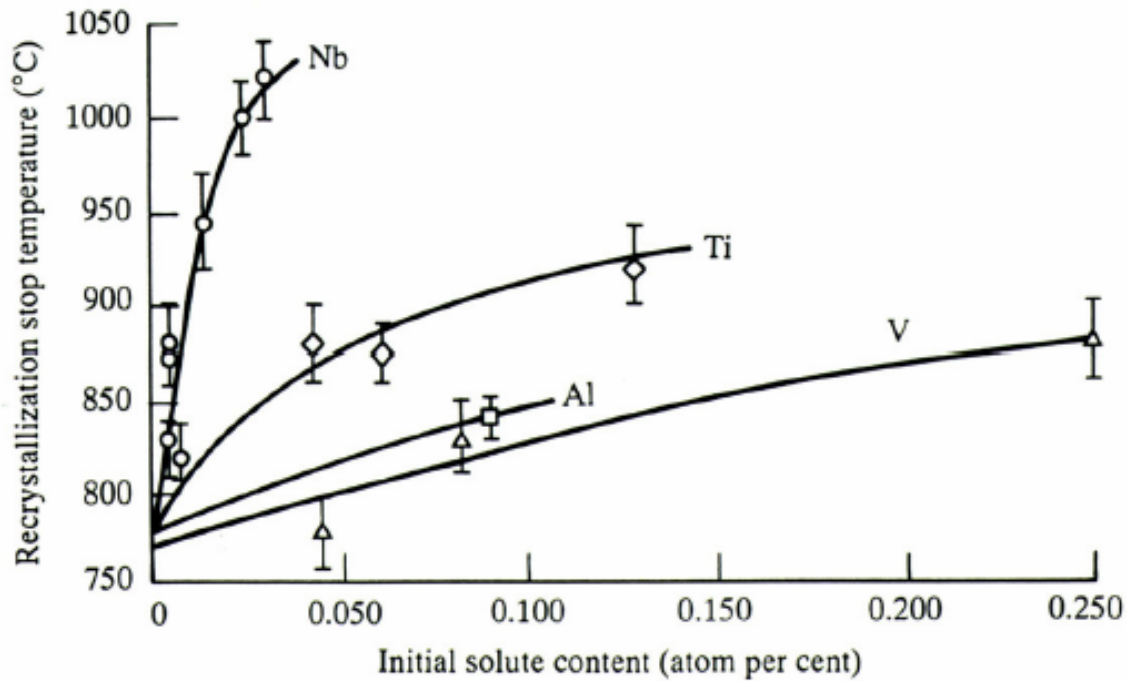


Figure 4 Plot of recrystallization stop temperature vs. solute content showing the effect of many different elements used in HSLA alloys

2.2.4 Cooling and Coiling

After the finishing passes are complete and the steel has left the rolling mills, the product is subjected to final cooling. During cooling the temperature is carefully controlled in order to achieve the properties desired. By controlling the temperature and cooling rate the desired final microstructure and properties are achieved. For instance, it has been found in NbV steels that

with higher controlled cooling rates the final rolling can occur at higher temperatures (800 °C) and achieve the same strength as though it were rolled at 700 °C and allowed to air cool. In addition the steel cooled quickly retains better toughness properties.¹² It is also important to understand that the cooling rate from rolling temperature can affect the transformation from austenite to ferrite, by lowering the temperature at which this transformation occurs. Lowering the transformation temperature then increases the driving force for the nucleation of ferrite. Furthermore, an increase in cooling rate promotes finer precipitate formation which in turn provides for better properties at room temperature. In continuous cooling scenarios, the cooling rate is limited by the need to allow ferrite and pearlite to form; this restriction is reduced when the cooling rate is decreased once a specified temperature is reached.⁵

In modern mills the cooling process happens in two parts. Initially, after the final hot rolling passes the strip is cooled rapidly (10-30 °C/s), usually to below the ferrite transition temperature. Once a predetermined temperature is reached this rapid cooling is then stopped at a temperature known as the 'coiling temperature.' From this the hot-strip is gathered into a coil, stored, and allowed to cool to ambient temperature at a much slower rate. This coiling procedure has become a necessity because of economic and industrial requirements, but also has its effects on the final product. For instance, by lowering the coiling temperature through longer periods of accelerated cooling, the yield stress can be increased through an enhancement of the structure formed during transformation. In turn, the slow cooling from the coiling temperature allows for beneficial effects, such as precipitation hardening and tempering of the hardened structure to take place.^{2, 13}

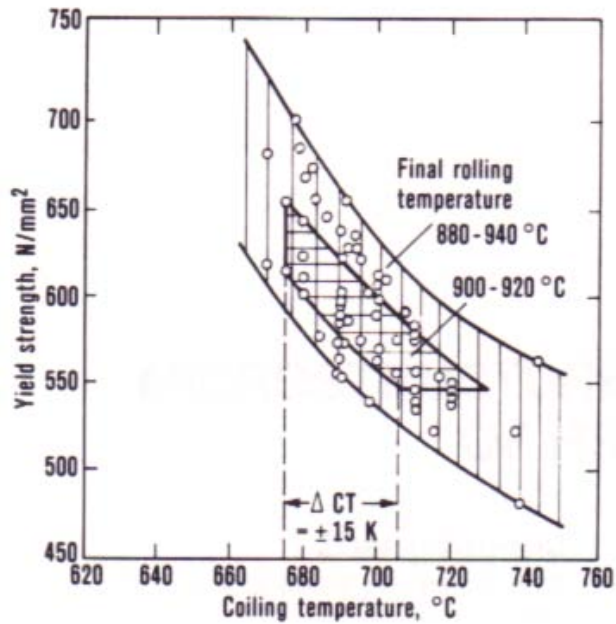


Figure 5 Effect of coiling temperature on Ti microalloyed steel

2.3 FORMATION OF FERRITE AND HIGH CARBON MICRO-CONSTITUENTS DURING TMP PROCESSING

As the hot-strip is allowed to cool from the final rolling temperature, transition temperatures for the formation of ferrite and other transition products such as bainite, pearlite, etc. are reached. Depending on the alloy content, the thermomechanical processing and the cooling procedures these microstructural components can form in varying amounts and combinations. Being able to predict exactly how the transformations occur has been found to be extremely complex due to the interactions of many different and sometimes competing processes.

In these steels, the formation of ferrite is usually controlled by way of the deformations of the austenite during the high temperature rolling passes. This is because ferrite nucleation

primarily occurs at sites in the austenite grain structure like grain boundaries, grain edges and corners, and dislocations.¹⁴ Therefore, the processes of roughing and finishing have the primary effect of promoting ferrite nucleation. However, due to the many other variables involved, polygonal ferrite is not always the only or even the primary product remaining after the transformation from austenite.

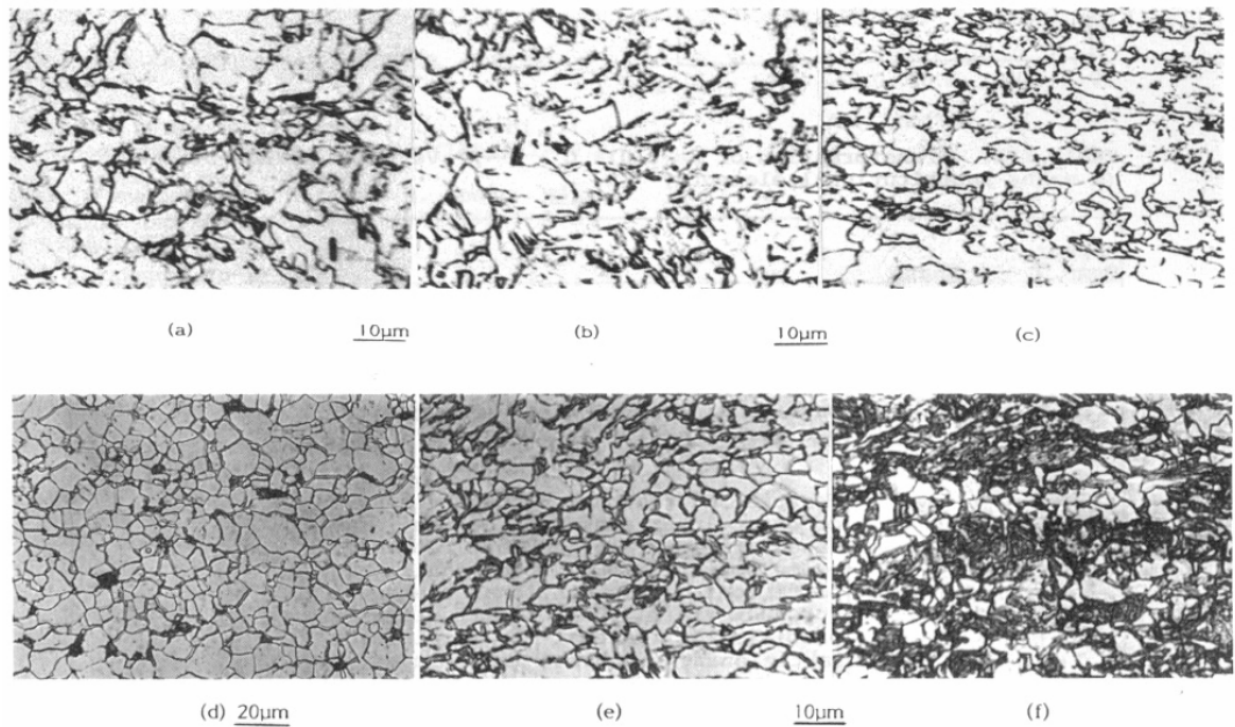


Figure 6 Examples of different types of microstructures possible under different processing conditions in HSLA Steels; a, b & c) Quasipolygonal Ferrite & Bainite d) fine polygonal ferrite & pearlite e) acicular & quasipolygonal ferrite f) quasipolygonal, bainitic, & acicular ferrite¹⁵

The figure above shows some microstructures that can evolve from the same steel simply through differences in the processing parameters. Present here are examples of polygonal, quasipolygonal, acicular and Widmanstatten ferrites. Also high carbon products can be observed like bainite, pearlite and martensite.

2.4 STRENGTHENING MECHANISMS

Modern steels attain strengths that were previously unachievable before the advent of micro-alloying. This significant improvement is possible through the interaction of multiple strengthening mechanisms. Solid solution strengthening contributes through the addition of elements that, when in solution, act by deforming the crystal lattice, strengthening the matrix. The precipitation of solute atoms into the bulk, either at grain boundaries or within the grain, can act as a direct barrier to both dislocation motion and grain boundary movement, further strengthening the steels. Finally, the evolution of techniques to refine grain size has allowed for a significant boost in both strength and toughness.

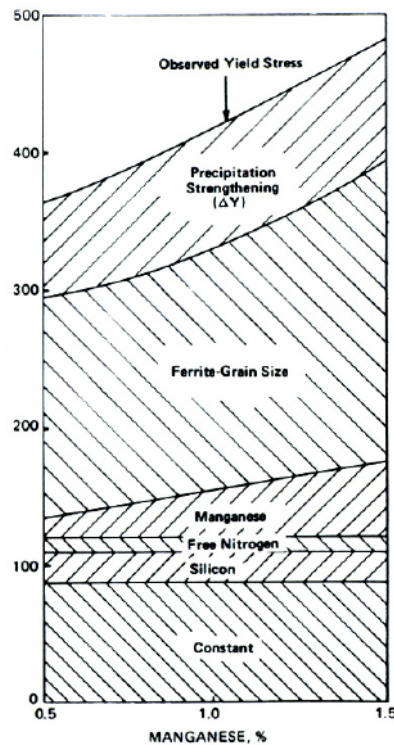


Figure 7 Diagram showing how many different factor contribute to the strengthening of manganese containing micro-alloyed steels¹⁶

2.4.1 Grain Size Strengthening / Hall-Petch Equation

It is known that ferrite grain refinement results in higher overall strength and toughness. This strengthening is said to occur because of how dislocations act as they approach the grain boundary. When a dislocation moves toward a grain boundary, its motion is hindered. This dislocation cannot usually move into another grain because, due to the approximately random orientation of the polycrystal, no similar slip plane exists in the adjacent grain.

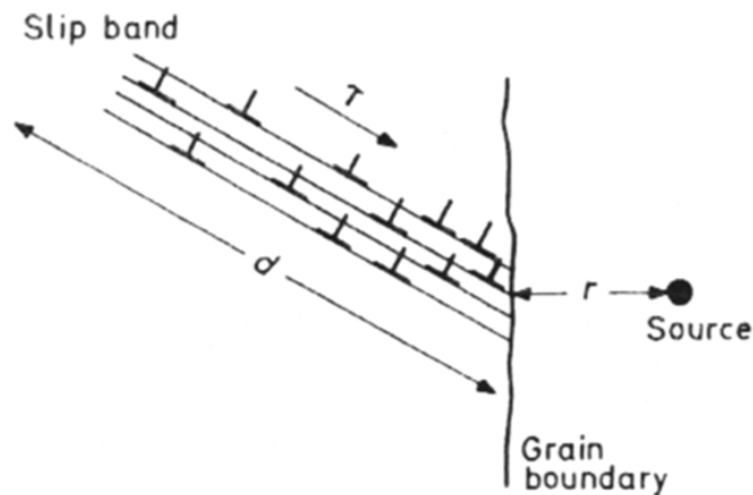


Figure 8 Illustration of dislocation pile up at the grain boundary

As more dislocations approach the dislocation already stopped near the grain boundary, stress is built up until eventually enough stress is exerted on an adjacent crystal so as to create dislocation sources in those grains as well. The stresses required to activate these dislocation sources are dependent on the size of the grain involved.^{17, 18}

Hall-Petch were able to develop a relationship between grain size and yield stress in a polycrystal.^{19, 20} Equation 2 shows that the yield stress, σ_y , is dependent upon σ_i , known as the lattice friction stress, which is the minimum stress needed for dislocation motion. The k_y term is a constant representing the increase in stress needed to spread dislocation motion and yielding from one grain to another. Finally, d represents the grain size.

$$\sigma_y = \sigma_i + k_y d^{-1/2} \quad (2)$$

The inverse square relationship with respect to grain size in the equation represents how larger grains can hold more dislocations; therefore, they need less stress in order to propagate yielding into the bulk.

It is well understood that a fine grain size is ideal and desired of all high strength steels. In order to achieve fine grain size a good understanding of how the ferrite microstructure evolves in any thermomechanical processing route becomes very important. Generally, the goal in any steel processing technique is to achieve as many ferrite nucleation sites as possible in order to achieve a fine grain size. Austenite grain boundaries as well as deformation bands in the austenite grain are considered the most important of these. Figure 9 shows the importance of deformed austenite structures in the final grain size. The figure also shows continued refinement with higher cooling rates.

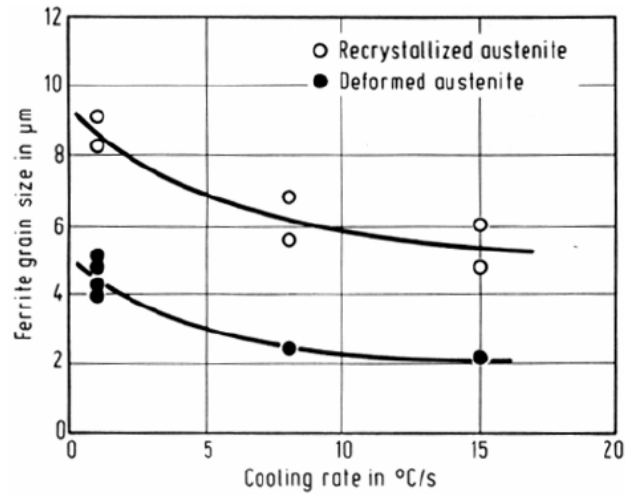


Figure 9 Effect of cooling rate on final ferrite grain size, shows conditions of both recrystallized and deformed austenite.

The importance of the deformed austenite was investigated by Hulka who used a parameter similar to S_v in order to quantify the deformation in the austenite. Hulka used the dimension of the austenite perpendicular to the rolling plane to develop an equation that described his observations.

$$d(\alpha) = 0.4 * h(\gamma) \quad (3)$$

Here $h(\gamma)$ is the austenite dimension variable and $d(\alpha)$ is the final ferrite grain size. This equation shows that the smaller the perpendicular dimension of the austenite the smaller the final ferrite grain size will be. Therefore, a deformed and ‘pancaked’ austenite structure is ideal for nucleating many small ferrite grains.²¹

Due to the nature of the many strengthening mechanisms that interact in steels, it is possible to modify the Hall-Petch equation to accommodate these mechanisms. This modification leads to a linear addition of many strengthening terms.

$$\sigma_y = (\sigma_i + \sigma_{sss} + \sigma_{pptn} + \sigma_{\perp} + \sigma_{sg} + \sigma_t) + k_y d^{-1/2} \quad (4)$$

The equation above shows terms for many different strengthening mechanisms added together, σ_{sss} , for solid solution strengthening, σ_{pptn} , for precipitation strengthening, and so on. Each of these may in turn have equations modeling their overall contribution to the yield stress.

2.4.2 Solid Solution Strengthening

The use of solute atoms plays an important part in the strengthening of HSLA steels. The primary role of these alloying additions is to increase the lattice friction thereby increasing the resistance to deformation in the ferrite crystal. By creating stresses within the lattice structure the solute can interact with dislocations, relieving some of the stresses induced by the dislocations. The two main types of solutes, interstitial and substitutional, each affect strength in different ways. Interstitial solutes are atoms that fit in between lattice points on the ferrite matrix. They have the most significant effects on strength, but their limited solubility restricts their ultimate effectiveness. Substitutional solutes, in contrast, replace Fe atoms in the lattice. Their solubility is much higher but their effectiveness and cost are such that abundant use of them is not particularly economical. The figure below shows the significant difference in how interstitial atoms (C, N) can strengthen steel versus how substitutional solutes (Cu, Mn, etc.) effect yield stress.

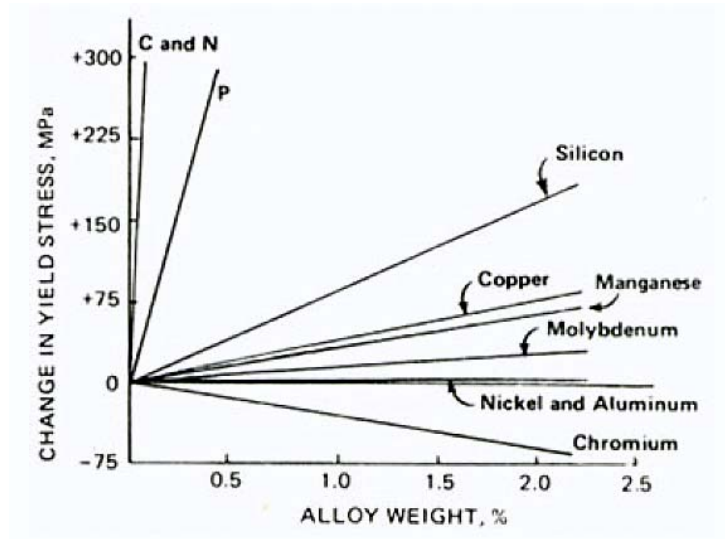


Figure 10 Effects of solid solution content on yield stress in low alloy steels ²²

The figure shows that the effects of each of these solutes in the yield strength of bulk multi-crystal material as well defined and linear, for both interstitial and substitutional solutes up until their solubility limits. These strengthening effects can be modeled linearly with a general equation such that;

$$\Delta\sigma_{ys(SS)} = \sum (\chi_i k_i) \quad (5)$$

Here, the total contribution to the yield strength of the steel due to the solid solution additions can be determined by the summation of the products of the weight percent of each solute (χ) by their strengthening coefficient (k).²³

2.4.3 Precipitation Strengthening

The strengthening effect of precipitation in steels has been thoroughly investigated for over half a decade. The effects of these small precipitates on the overall strength can be attributed to multiple mechanisms. Ashby and Orowan were some of the first to observe and

quantify the effects of incoherent precipitates pinning dislocation motion. This mechanism is known as dispersion strengthening.^{24, 25} Others later identified more mechanisms contributing to strength. For example, Coherency Strengthening,²⁶ Chemical (Anti-phase) Strengthening,²⁷ and Particle Shearing²⁸ have all been found to play roles in how precipitates participate in the strengthening of steel.

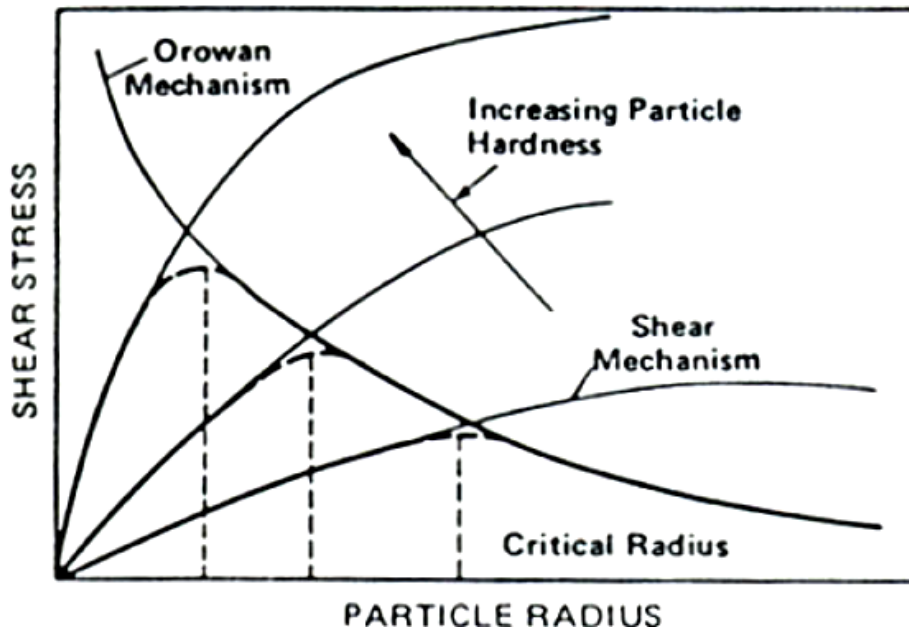


Figure 11 Depending on particle size, hardness, and applied stress different mechanisms provide strengthening through precipitation.

Each of these mechanisms provides strengthening in different ways. Particle cutting and the bowing of dislocation loops (Orowan mechanism) are the two systems which show to be the most effective at increasing strength, while chemical hardening occurs generally as a result of particle cutting.

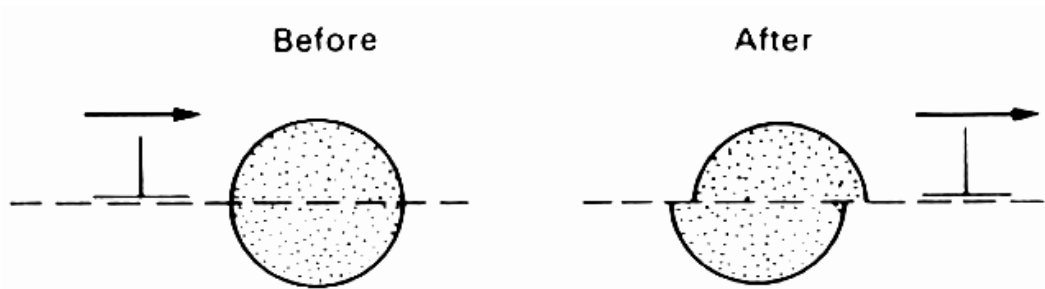


Figure 12 How dislocation motion through a particle shears the particle creating antiphase boundaries.

The particle shearing (or cutting) effect, shown in figure 12, occurs when dislocations move through the particles as they slip through the crystal lattice. This cutting usually happens when the particles are small or soft. Many factors act as the source of strengthening for this type of mechanism including; coherency strain, stacking fault behavior, and modulus effect.²⁹ In the case of coherency strain, the mismatching between the atoms in the matrix and those of the particles create a strain affecting the dislocation as it passes from the bulk to the particle.³⁰ Next the difference in stacking fault energies between particle and bulk can lead to strengthening where if the particle is more likely to create extended stacking faults with respect to the matrix this can have a significant effect. Finally, in some cases, once particles are sheared and an antiphase boundary is created between the particle and the bulk differences in modulus between the two impede the dislocation motion they pass through these boundaries.^{31, 32}

While particle shearing cannot be entirely ruled out in these low alloy steels, the high hardness of the particles most often identified in HSLA suggests that the Orowan, or dispersion-strengthening, process is at work.

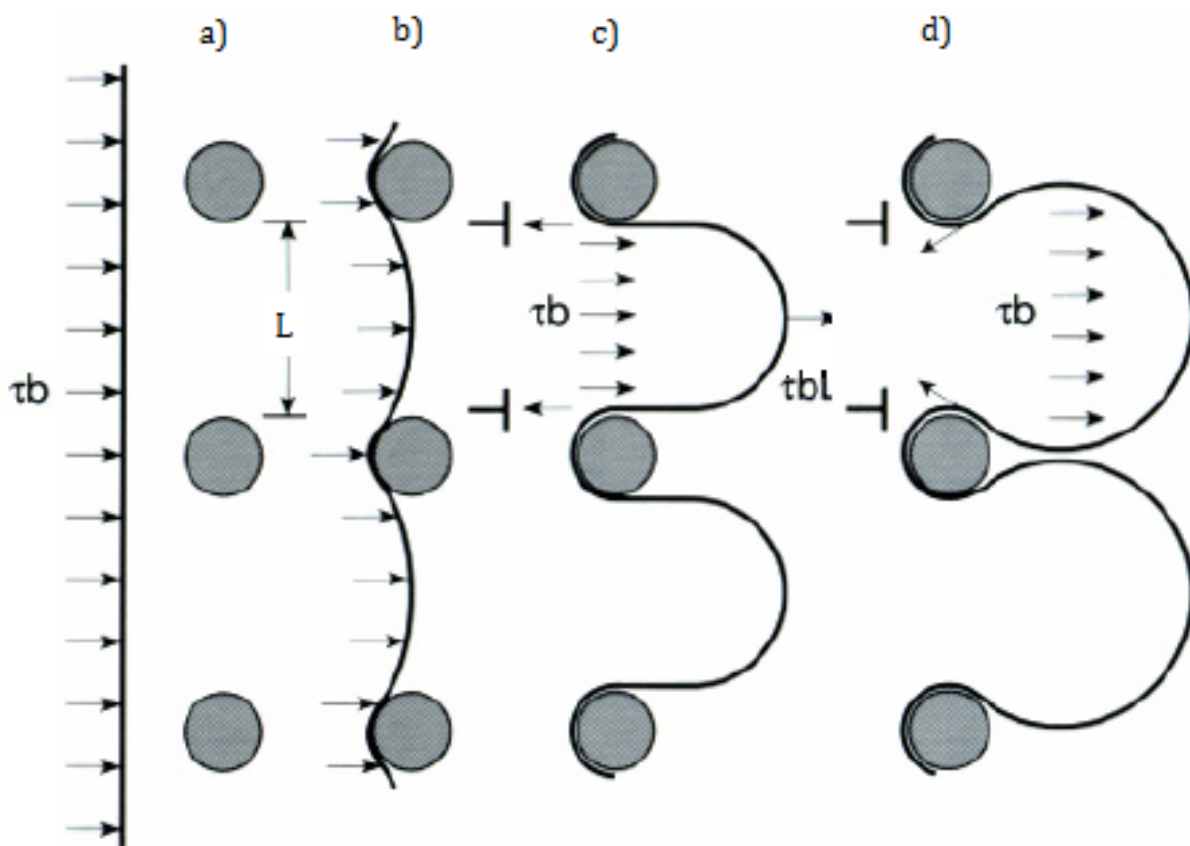


Figure 13 Depiction of how hard particles lead to Orowan bowing of dislocation particles. a) approach, b) sub-critical, c)critical, d)escape

Figure 13 shows the effect that these small hard particles have on a dislocation line. In the Orowan process, when a force is applied the dislocation begins to move under the stress, as the dislocation moves toward an array of particles (a) the dislocation line has a tension per unit length of τb . When the line finally reaches the particles (b) the motion of the dislocation is halted as the line begins to bow around the particles in order to achieve a force balance. At this point, in order for the dislocation to continue its motion through the lattice the dislocation line must increase in length, increasing the amount of or stress required to move it (c). From here on, as stress increases, the dislocation continues to bow around the particles (d) until; finally, the loops escape the particle array and can continue through the crystal.³³ This behavior was

modeled by Ashby-Orowan and a mathematical relationship was developed, as shown in equation 6.³⁴

$$\sigma(MPa) = \frac{5.9\sqrt{f}}{x} \ln\left(\frac{x}{2.5 \times 10^{-4}}\right) \quad (6)$$

This equation shows that the size (x) and volume fraction (f) of these particles are the primary factors in developing strength through dispersion. Therefore, as particle size decreases and volume fraction increases so does the yield stress of these steels.

3.0 STATEMENT OF OBJECTIVES

This research is being carried out in order to understand and develop accurate and effective laboratory TMP methods for simulating the effects of a hot-strip process on the resulting final microstructure. For this purpose, an investigation in three parts has been conducted, each part with specific objectives and goals.

First, a comprehensive and systematic characterization of the microstructure of the four commercial as-hot rolled HSLA (350 – 420 MPa YS) steels provided by the sponsoring company of this project. The microstructural investigation was conducted, to better understand the relationship between the current processing and the final microstructure. This characterization includes data from Optical, and Electron Microscopy as well as the results from Electron Backscatter Diffraction and Vickers hardness testing

The next objective was an understanding of the transformations which occur in these steels during cooling from the finishing temperature was needed. This understanding comes from a combination of computer models used to create continuous cooling transformation maps, and dilatometric cooling studies to experimentally observe these transformations in the hot band.

Finally, thermomechanical process (TMP) simulations were carried out. The starting condition for these experiments was the transfer bar material. The major objective of this part of the study was to investigate how the final rolling temperature, cooling rate, and coiling temperature conditions affect the final microstructure of these steels.

4.0 EXPERIMENTAL PROCEDURE

4.1 MATERIALS

Commercial samples from 350 – 420 MPa HSLA steels were received for this investigation. Both transfer bar and hot rolled materials of four different alloys were provided. The chemical composition of the steels is presented in Tables 1 and 2.

Table 1 Chemical composition of transfer bar samples received and subjected to thermomechanical processing simulations

Grade	C	Si	Mn	S	P	Al	Nb	V	Ti	B
7045	0.080	0.10	1.14	0.003	0.014	0.04	0.03	0.00	0.019	-
7153	0.290	0.13	1.35	0.015	0.018	0.03	0.00	0.00	0.038	44.00
7631	0.180	0.03	0.67	0.008	0.008	0.035	-	-	0.019	-
7038	0.061	0.031	0.806	0.005	0.007	0.04	0.017	-	0.017	-

Table 2 Chemical composition of hot band samples subjected to microstructural analysis and continuous cooling studies

Coil number	C	Si	Mn	S	P	Al	Nb	V	Ti	Grade
263677	0.058	0.032	0.773	0.0057	0.0137	0.034	0.0153	0.0016	0.0147	7038
263684	0.054	0.03	0.79	0.0012	0.0088	0.048	0.0184	0.0019	0.0157	7038
263655	0.0643	0.0756	1.1218	0.0053	0.0121	0.0396	0.0349	-	0.0212	7045
272174	0.299	0.158	1.387	0.0012	0.011	0.029	-	0.00311	0.0416	7153
272244	0.158	0.035	0.657	0.003	0.012	0.027	0.0032	0.0009	0.157	7631

4.2 CONTINUOUS COOLING STUDIES

Both computer simulations as well as experimentation were used to determine the effect of cooling rate on the hot band material. A thermodynamic J-MAT Pro software package was used to determine the theoretical continuous cooling transformation temperatures for the steels provided. Then, dilatometry samples, see Figure 14, were machined from the as-received hot band material. Dilatometric studies in a Theta High Speed Dilatometer from each of the alloys received were conducted. Each dilatometry sample was reheated to a given austenite temperature held for fifteen minutes and then cooled at rates of 0.1, 1.0, and 10 C/s. The transformation behavior was recorded and the corresponding transformation temperatures during cooling were assessed and recorded.

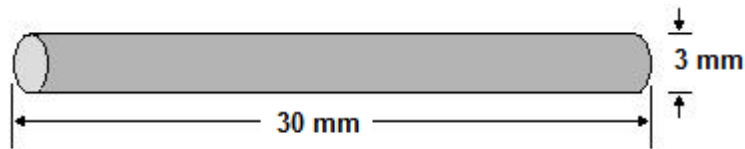


Figure 14 Drawing of dilatometer sample

4.3 THERMOMECHANICAL PROCESSING SIMULATIONS

In the thermal-mechanical processing studies of the alloys, effects of both coiling temperature and cooling rate to the coiling temperature were examined. The TMP studies were conducted using a high temperature computer controlled MTS-458 compression test machine with the capability of deformation under constant true-strain rate conditions. Cylindrical

specimens of 0.5” diameter and 0.75” length were machined from the transfer bar material. The temperature was monitored via a thermocouple placed in a hole of 1/16” diameter drilled into the cylinder at half height. In addition, the modified Rastegaev design was used for the compression specimens in order to decrease instances of barreling and to reduce rolling friction. Figure 15 shows a schematic of this modified Rastegaev design.³⁵

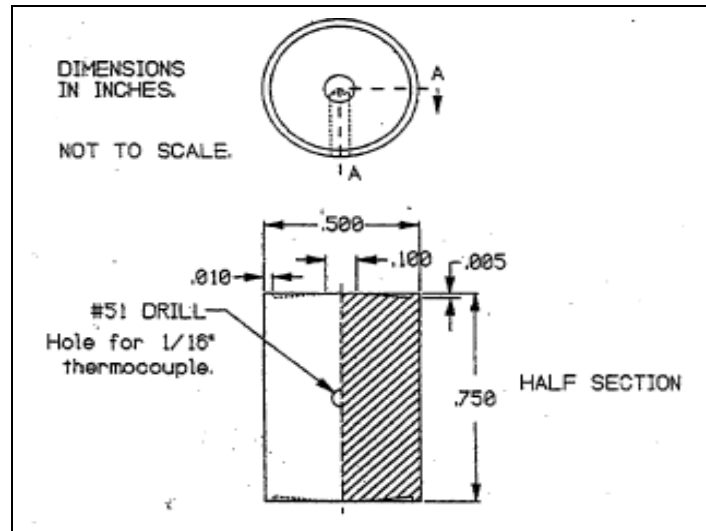


Figure 15 Schematic Drawing of Rastegaev modified compression sample for use in thermomechanical processing simulations

For these tests, the samples were made from the transfer bar material, each sample was encapsulated under vacuum in a sealed quartz tube, reheated to 1250 C in a radiant heat furnace held for an hour and then quenched. Then, in preparation for the compression test, each sample was coated using an electroless nickel plating process.³⁶ Finally, each sample was subjected to a simulated hot rolling process using the MTS compression testing apparatus.

An experimental design procedure was established for each alloy system. The procedure followed during the simulation was as follows;

- Each sample was heated to 1250 C and held for 2 minutes
- Samples were cooled to the first rolling temperature and deformed with a 50% reduction
- Further cooling to the final rolling temperature and deformed with a 50% reduction again
- Samples were then cooled at 30 Or 10 °C/s to the prescribed coiling temperature
- Finally each sample was cooled from the coiling temperature to room temperature at a rate of 30 C/hr

A constant true-strain rate of 10^{-2} sec^{-1} was used. A schematic of the process is shown in figure 16 below.

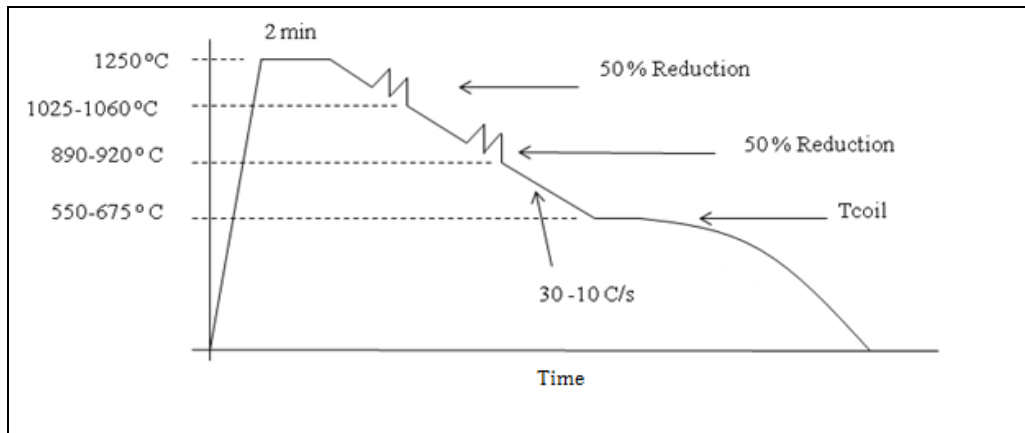


Figure 16 Schematic of TMP process showing approximate temperature range for each step of the process. After Tcoil, the slow cooling to room temperature is depicted as sloping curve toward the horizontal axis.

Each alloy differed in composition, so the processing temperatures and coiling temperatures were different for each grade, table 3 shows the parameters used for each grade of steel being examined.

Table 3 Matrix of parameters used in running TMP simulations

Grade	First Rolling Temp	Final Rolling Temp	T coiling (°C)	Cooling Rate (°C/s)
7045	1024	901	550	10
			600	30
			650	
7153	984	889	650	10
			750	30
7631	984	889	550	10
			650	30
7038	1024	901	550	10
			650	30

4.4 FINISHING ROLLING TEMPERATURE STUDY

After some discussion of initial results it was decided that, for the steel grade 7038, a study of the effect of final rolling temperature was needed. For this, an extra set of TMP simulation tests were run using the 7038 transfer bar material. In this case, the final rolling temperature was 870 °C in place of 901 °C. All conditions run during the TMP were also run with this new rolling temperature and a comparison analysis made.

4.5 EXPERIMENTAL TECHNIQUES AND MICROSTRUCTURAL ANALYSIS

4.5.1 Optical Microscopy

Optical microscopy was used to characterize the microstructure of the samples at all stages of the process. Hot rolled samples were cut perpendicular to the rolling plane and compression samples were cut parallel to the compression axis. Samples were all mounted in Bakelite and ground using abrasive papers, starting from 180 grit and gradually increased to 600 grit. Then samples were polished using 1 micron and 0.05 micron alumina pastes. Finally, samples were etched using a 3% Nital solution for 10-15 seconds.

Using a microscope connected to a computer, the Bioquant software was used to determine the ferrite grain size and volume fraction of the microconstituents. The ferrite grain size was determined by using the software's automatic measuring capabilities by manually tracing at least 200 individual grains for each sample. Volume fraction was determined by using the programs color threshold capabilities, with some manual adjustments, along with the automatic measuring process.

4.5.2 Scanning Electron Microscopy and EBSD-IQ

In order to obtain high quality high magnification images and better identify the phases present, the optical microscopy samples were re-polished and etched for slightly less time then coated with palladium and placed in the scanning electron microscope, where images with magnifications as high as from 1000 to 10000 times were taken.

Also, electron backscatter diffraction was used to further characterize the samples. For the EBSD analysis samples were ground and etched in the same way as for optical microscopy except a final vibro-polishing step is added before the sample is placed in the SEM and the diffraction test is run.

In modern HSLA steels, multiple microconstituents are often present in any given sample. The presence of these microstructural features are usually easily identified using traditional SEM and optical microscopy, but the actual volume fraction is difficult to quantify using traditional metallographic techniques. This is why EBSD-IQ was used in this study.

In EBSD-IQ analysis the microstructure is easily quantified using a value recorded during traditional EBSD analysis known as image quality (IQ). Image quality is a quantification of the sharpness of the Kikuchi pattern produced. This sharpness is related to the degree of lattice imperfection, or crystalline defects, of the sample. For example, an elastically distorted lattice will have a Kikuchi pattern which appears unfocused and unclear and its IQ value will be low, see figure 17 below.

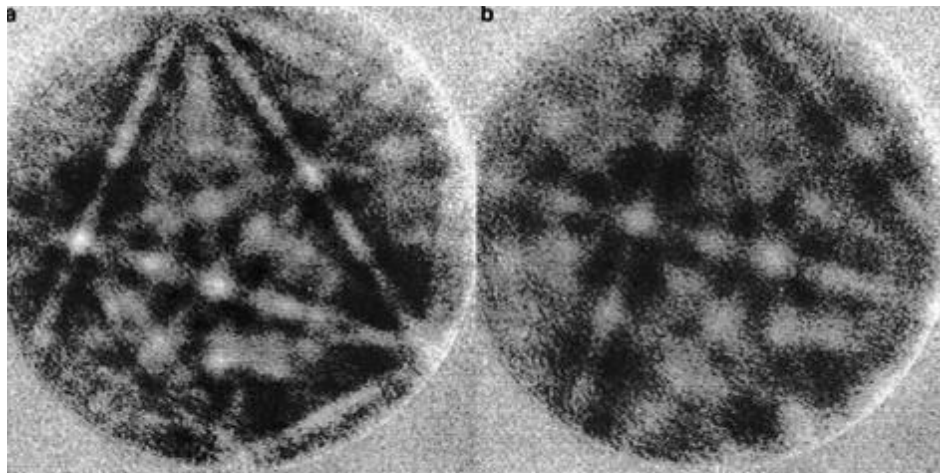


Figure 17 Two Kikuchi patterns showing how difference in lattice distortion can affect the image quality of the diffraction pattern (a) Ferrite, with high IQ (b) Martensite, with low IQ.

The IQ method used to characterize the microstructure of these samples is able to eliminate the contribution from grain boundaries, which is something that can be a problem using optical metallography. Depending on the phase and the defect structure of each grain, such as dislocation density, the IQ is measured and analyzed as a full distribution of values in a given sample. Also, a normalization procedure is used to minimize the effects of image processing. Then, a computer program is used to identify grain boundaries on the IQ distribution. The program then eliminated the grain boundary data and creates a curve and using a multi-peak model for allows for the analysis of the multi-component microstructures.^{37, 38}

4.5.3 Transmission Electron Microscopy (TEM)

Some hot band samples were further examined using the TEM technique in order to study and characterize any precipitation that might be present due to the addition of niobium. For this purpose, the JEM-200CX electron microscope was used, and was operated at 200 kV. Thin foils were prepared for use in the TEM for this analysis. The preparation of the thin foils began by cutting thin strips of from the hot band parallel to the rolling direction about 0.8 mm thick. After cutting the strips from the stock material, they were then thinned by mechanical grinding using papers with a very fine grit of 2400 to strips less than 0.4 mm in thickness. Next, 3mm diameter discs were punched from these thin strips and these were then chemically thinned and polished using a twin-jet polisher with an electrolytic solution made from 80g of sodium chromate (Na_2CrO_4) in 400 ml of acetic acid (CH_3COOH).³⁹

4.5.4 Microhardness

As part of the microstructural characterization of the samples, microhardness tests were run on all optical microscopy samples. A Leco M-400 G microhardness tester was used along with a square pyramid diamond indenter. The tester was put on the 500 gram setting and set for a test time of 7 seconds, and using a microscope connected to a computer with the Omniment program the hardness values were automatically calculated by manually measuring the indentation size.

5.0 RESULTS

Commercial transfer bar and hot band samples of the four different high strength low alloy steels to be investigated in this research were used in the thermomechanical processing simulations while the hot band material was used for the systematic microstructural analysis of the microstructure. Samples machined from the hot band condition were then used in the dilatometric studies to help develop transformation data for the steels being studied.

5.1 HOT BAND MICROSTRUCTURAL ANALYSIS

Using low and high magnification optical micrographs of each of the four alloys along with the Bio-Quant software a preliminary analysis of the microstructure was made. In addition to the optical analysis, the microhardness of each hot band sample was measured. For each of the alloys, multiple samples of hot band material were analyzed. In each case the conditions of each sample was somehow different. The CSP or CP value given in the coil identification pertains to either the location in the coil where the sample was taken, or if it was taken after the sample had been subject to a skin pass process. In the case of alloy 7038 samples of two different coils were received and examined.

In order to obtain a better understanding of the nature of the microstructure the scanning electron microscope was used to attain high quality imaging of the micro-constituents. Also the electron backscatter diffraction – image quality (EBSD-IQ) method was used to attain a quantification of the microconstituents present in the hot band.

5.1.1 Hot Band Analysis of 7045

Initial optical microscopy of the hot band for grade 7045 was taken from the hot band samples 163655 csp1 and 163655 csp4. From the initial optical microscopy of these samples show a very fine ferrite grain structure with some non-polygonal ferrite grains observable. Otherwise, very little of the total area observed showed other microconstituent or secondary phase particles.

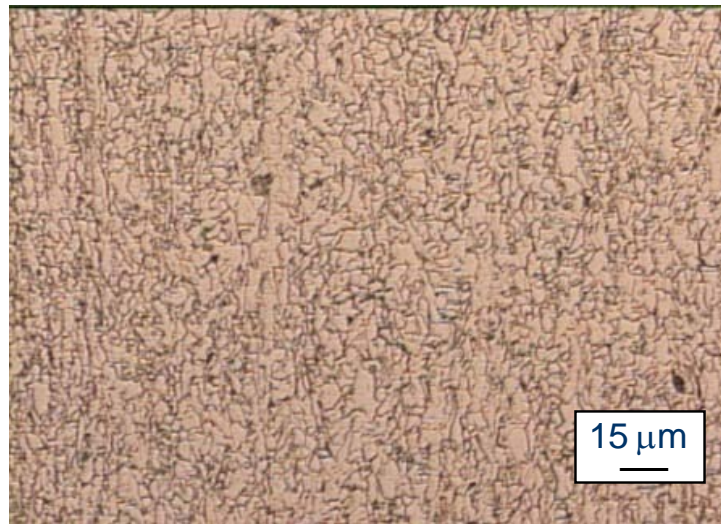


Figure 18 Optical micrograph of the ferrite microstructure in 163655 csp4, prepared using 3% Nital solution

The optical micrographs, of the 7045 hot band, were then used to conduct a microstructural analysis. Table 5 shows the results of this analysis including microhardness measurements.

Table 4 Chemical Composition of 7045

Grade	C	Si	Mn	S	P	Al	Nb	V	Ti	B
7045	0.080	0.10	1.14	0.003	0.014	0.04	0.03	0.00	0.019	-

Table 5 Results from the microstructural analysis of 7045 hot band materials

Coil ID Info	163655 CSP1	263655 CSP4
Grade	7045	7045
Average Grain Size (µm)	2.75	2.95
% Ferrite	98.5	99.7
Hardness	188.7	189.4
Std Dev	3.4	2.6

The higher magnification SEM images, likewise, show polygonal and non-polygonal ferrite grains. Upon closer examination the secondary particles observed under optical magnifications appear to be high in carbon without the identifiable lamellar structure of pearlite.

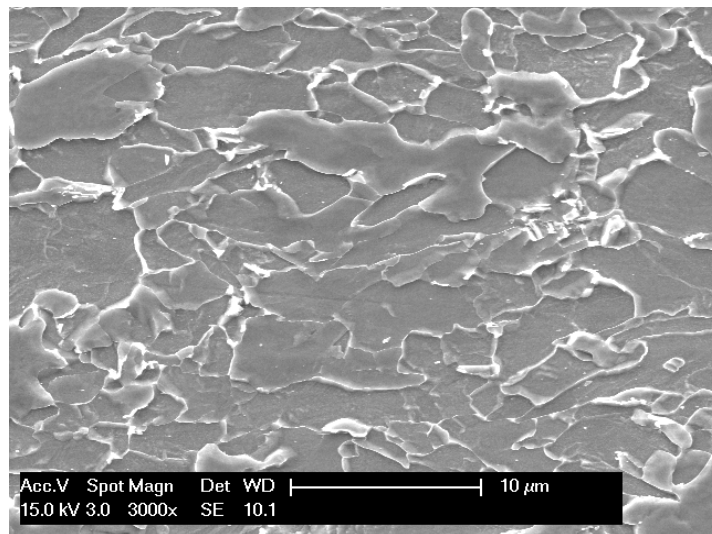


Figure 19 Secondary electron micrograph showing the microstructure in 163655 csp4 hot band material.

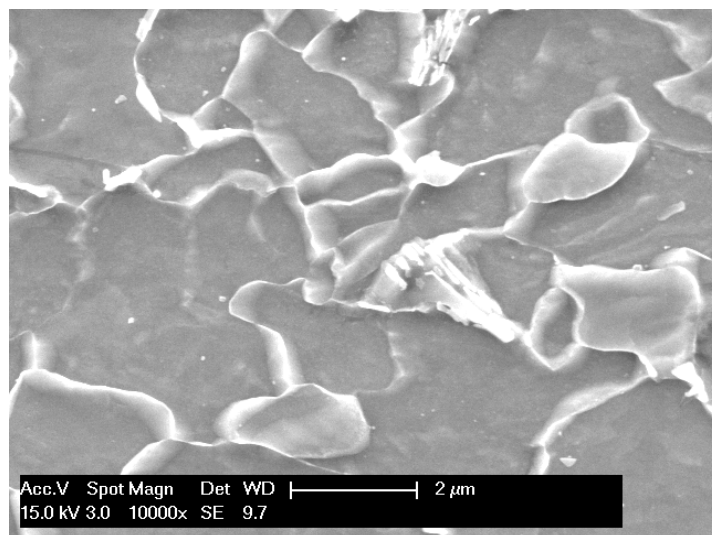


Figure 20 High magnification Secondary electron micrograph of 163655 csp4 hot band material showing secondary phase particle (very fine carbides).

From the IQ analysis of the EBSD data, it is clear that three phases are present. The EBSD-IQ distribution in the graph below shows that three peaks were identified each corresponding to a polygonal ferrite, acicular ferrite, and finally a low IQ peak representing the high carbon secondary phase observed in the micrographs.

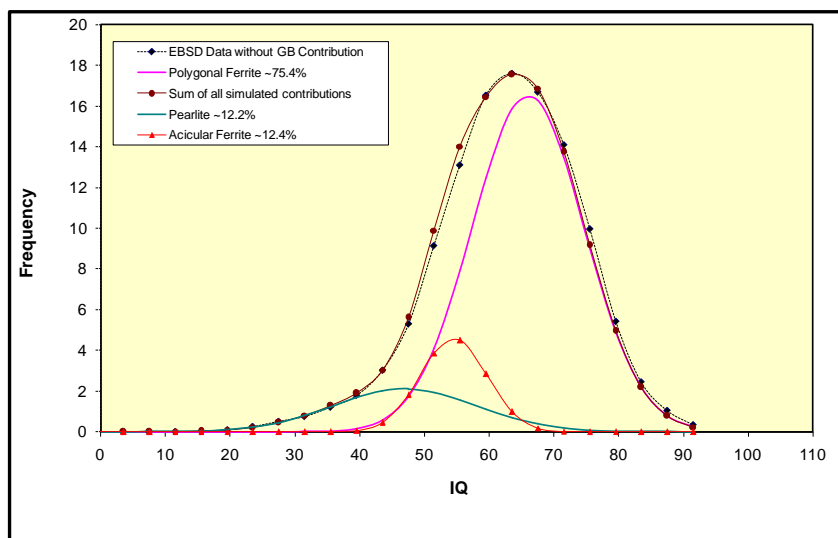


Figure 21 EBSD-IQ distribution curve for 7045 Hot band material showing peaks for each phase identified

From the micrographs and EBSD-IQ analysis a phase balance was constructed for the hot band material of 7045 and is shown in the table below.

Table 6 Results from EBSD-IQ analysis of 7045 hot band material

Steel Grade	α (Polygonal Vol.%)	α (Acicular Vol.%)	Pearlite (Vol.%)	High Carbon Constituents (Vol.%)
7045	75.4	12.4	-	12.2

For this grade, due to the presence of niobium in the composition, in addition to these microstructural observations a TEM analysis was made. Figure 22 shows the bright and dark field TEM images of a 7045 grain showing very few and extremely small precipitates. The precipitates were analyzed as NbC. The presence of these particles is very sparse and many grains do not appear to contain them.

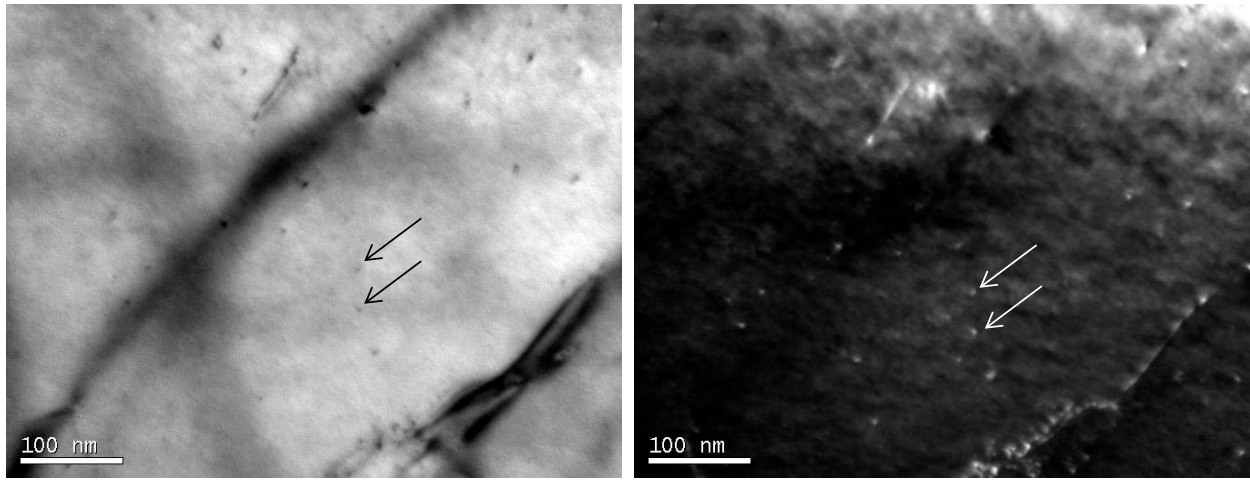


Figure 22 Very high magnification TEM images of 7045 hot band material, with arrows showing 2 examples of the very few well dispersed particles, shown in both bright and dark field conditions.

5.1.2 Hot Band Analysis of 7038

Initial optical microscopy of the hot band for grade 7038 was taken from the hot band samples 263677 csp4 and 263677 cp5, as well as, 263684 csp4 and 263684 cp5. In comparison to 7045 the ferrite grain structure is coarser and there is no immediate observation of any non-polygonal ferrite. The secondary phases present are generally in larger sized colonies than those found in 7045 but still take up very little of the total observed area. However, as in 7045 the nature of these colonies is not directly identified using optical microscopy.

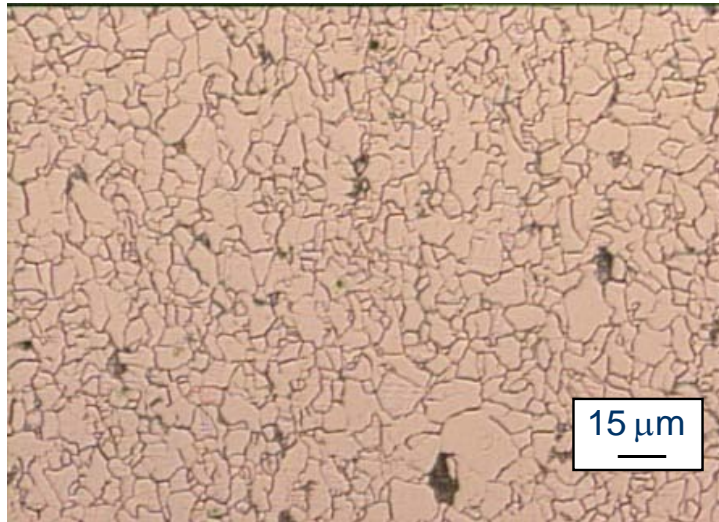


Figure 23 Optical micrograph of the ferrite microstructure in 263677 csp4, prepared using 3% Nital solution

Using these observations and micrographs, a thorough analysis of the optical microstructure in the hot band of 7038 was conducted. Table 8 has the results from this analysis.

Table 7 Chemical composition of 7038

Grade	C	Si	Mn	S	P	Al	Nb	V	Ti	B
7038	0.061	0.031	0.806	0.005	0.007	0.04	0.017	-	0.017	-

Table 8 Results from the microstructural analysis of 7038 hot band materials

Coil ID Info	263677 CSP4	263677 CP5	263684 CSP4	263684 CP5
Grade	7038	7038	7038	7038
Average Grain Size (μm)	4.15	4.4	4.25	4.65
% Ferrite	94.6	93.6	94.1	93.7
Hardness	146.8	168.6	151.2	151.5
Std Dev	6.4	15.4	5.7	5

Using the electron microscope the higher magnification, and better contrast and resolution the larger secondary phases are immediately identified with the characteristic lamellar structure exhibited in pearlite.

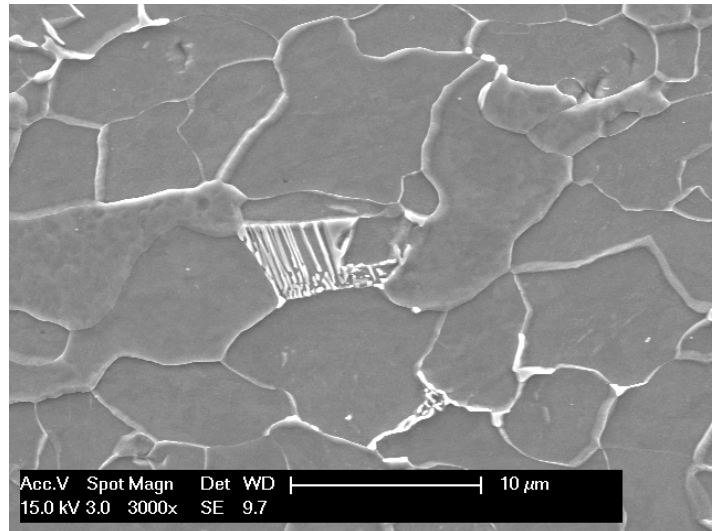


Figure 24 Secondary electron micrograph showing the microstructure the secondary phase in the 7038 hot band material.

The EBSD-IQ graph shown in Figure 25 shows two distinct peaks, the first easily identified as Polygonal ferrite and the other as carbon-rich or pearlite.

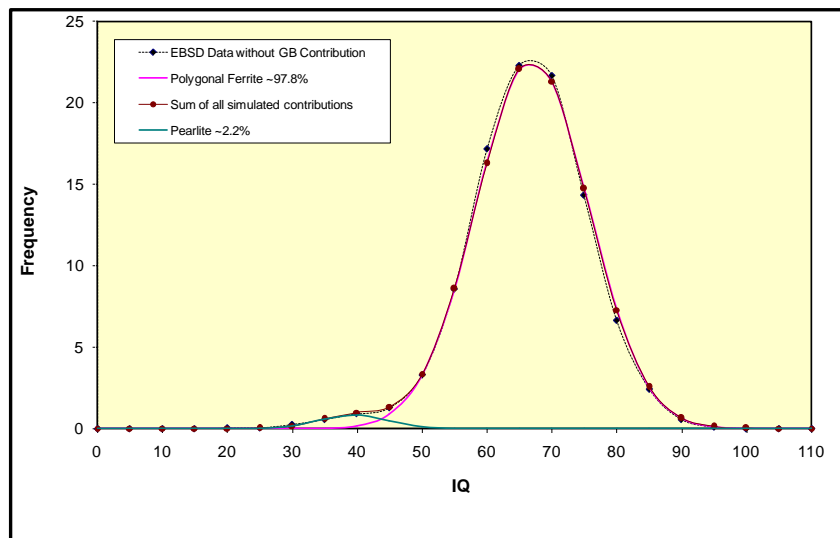


Figure 25 EBSD-IQ distribution curve for 7038 Hot band material showing peaks for each phase identified

The following table shows the results from the analyses made from combining the observations made with the SEM as well as the EBSD-IQ data. This information was used to create the phase balance seen in table 9.

Table 9 Results from EBSD-IQ analysis of 7038 hot band material

Steel Grade	α (Polygonal Vol.%)	α (Acicular Vol.%)	Pearlite (Vol.%)	High Carbon Constituents (Vol.%)
7038	97.8	-	2.2	-

Similarly to 7045, this grade was also subjected to TEM analysis. Figure 26 shows two TEM images of the same area taken in the bright and dark field of 7038. During this observation very few grains showed any precipitation. In the cases where particles were found they were small and dispersed as seen in the figure.

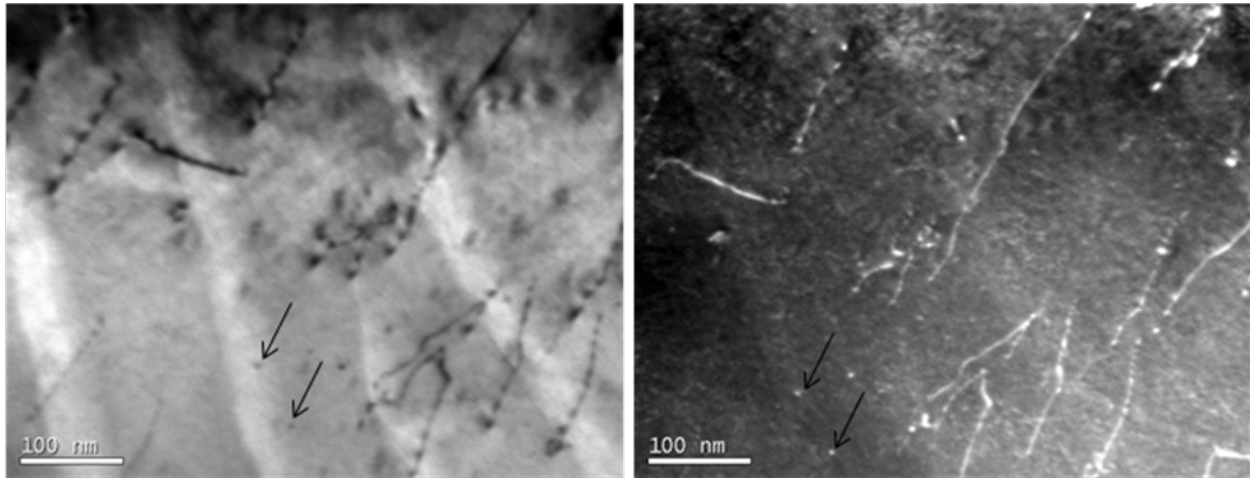


Figure 26 Very high magnification TEM images of 7038 hot band material, with arrows showing 2 examples of the very few well dispersed particles, shown in both bright and dark field conditions.

5.1.3 Hot Band Analysis of 7153

For the hot band analysis of grade 7153 the coils identified as 272174 csp1 and 272174 csp4 were prepared and used. Optical microscopy of 7153 reveals an obviously banded structure, with a high quantity of this banded structure. The ferrite grains are large, and have two distinct shapes. Some ferrite grains have an elongated shape while others are more regular and round. In some cases lamellas in the secondary phase are observable even with optical magnifications.

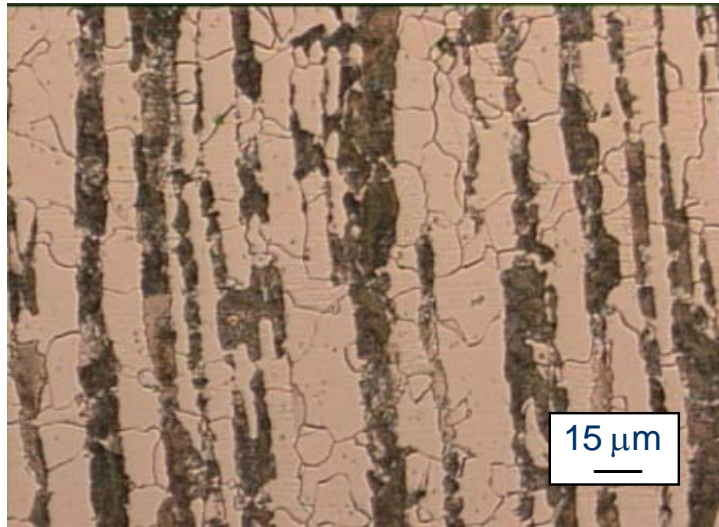


Figure 27 Optical micrograph of the ferrite microstructure in 272174 csp4, prepared using 3% Nital solution

From the microstructural analysis of 7153 hot band material results were compiled and are shown in table 11.

Table 10 Chemical composition of 7153

Grade	C	Si	Mn	S	P	Al	Nb	V	Ti	B (ppm)
7153	0.290	0.13	1.35	0.015	0.018	0.03	0.00	0.00	0.038	44.00

Table 11 Results from the microstructural analysis of 7153 hot band materials

Coil ID Info	272174 CSP1	272174 CSPP4
Grade	7153	7153
Average Grain Size(μm)	8.05	9.0
% Ferrite	43.4	45.7
Hardness	190	177.3
Std Dev	13.9	8.3

With the SEM microscopy analysis, the pearlite observed in only some of the secondary phase under the optical microscope, is found to be by far the predominant secondary phase observed.

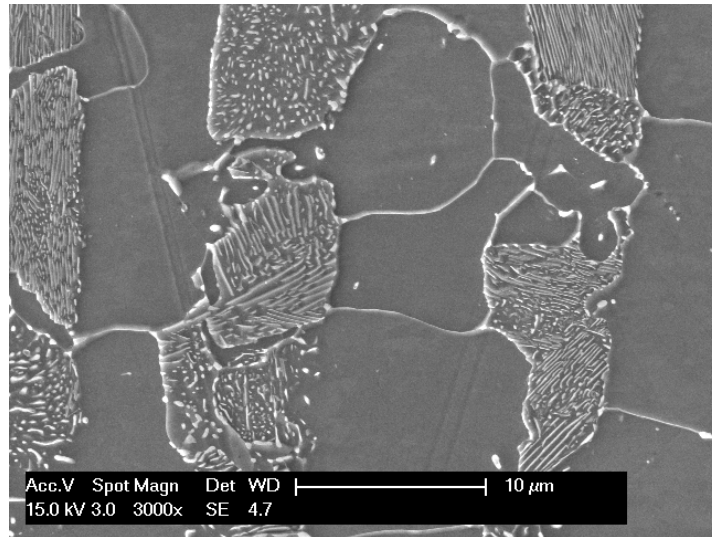


Figure 28 Secondary electron micrograph showing the microstructure and secondary phase in the 7153 hot band.

Due to the extreme heterogeneous nature of the 7153 hot band, two different diffraction tests were run and the results were averaged. The figures below show IQ results from the two separate EBSD tests. Each distribution shows peaks for polygonal ferrite, pearlite and the lower IQ peaks for high carbon constituents. The distribution in figure 30 shows two distinct high IQ peaks both of which have been identified as coming from polygonal ferrite. Also, in both figures a peak appears at very low IQ values, these peaks have been attributed to very high carbon enriched areas within these steels.

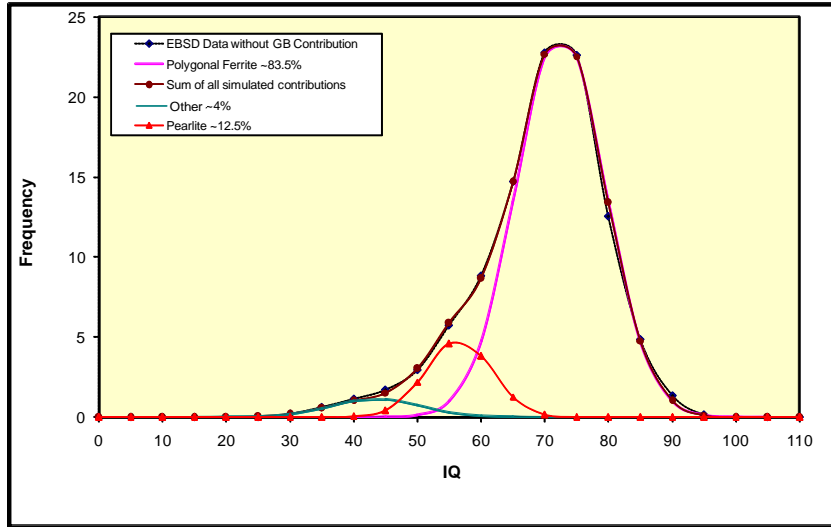


Figure 29 EBSD-IQ distribution curve for 7153 Hot band material showing peaks for each phase identified, 1 of 2.

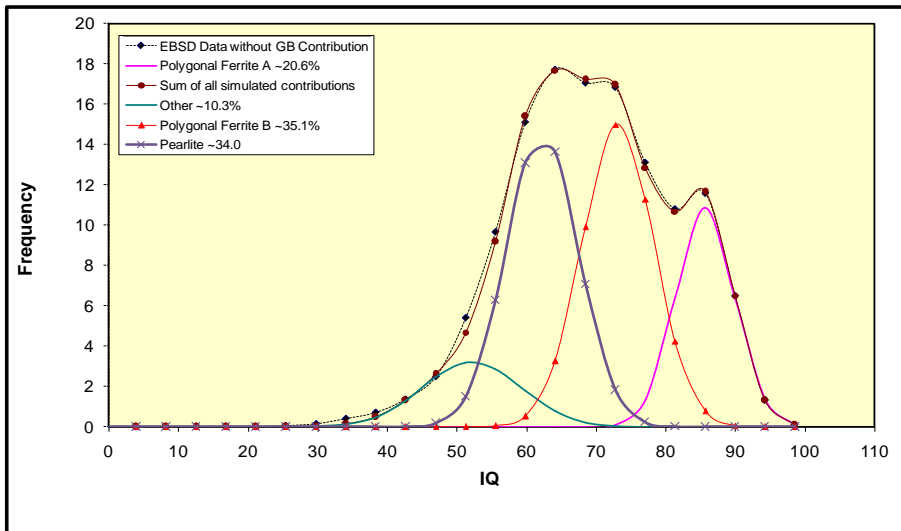


Figure 30 EBSD-IQ distribution curve for 7153 Hot band material showing peaks for each phase identified, 2 of 2

The tables below shows the values obtained from the analyses made from the hot band of 7153.

Table 12 Results from EBSD-IQ analysis of 7153 hot band material

Steel Grade	α (Polygonal Vol.%)	α (Acicular Vol.%)	Pearlite (Vol.%)	High Carbon Constituents (Vol.%)
7153	69.6	-	23.3	7.1

5.1.4 Hot Band Analysis of 7631

The hot band material used in this analysis of the 7631 grade steel came from the coil samples 272244 csp4, and 272244 cp5. The optical micrographs of this steel show a comparatively intermediate grain size with both polygonal and non-polygonal ferrite observed. More significant amounts of a secondary phase are observed than in both 7045 and 7038, but less than that of 7153 and with no apparent banding.

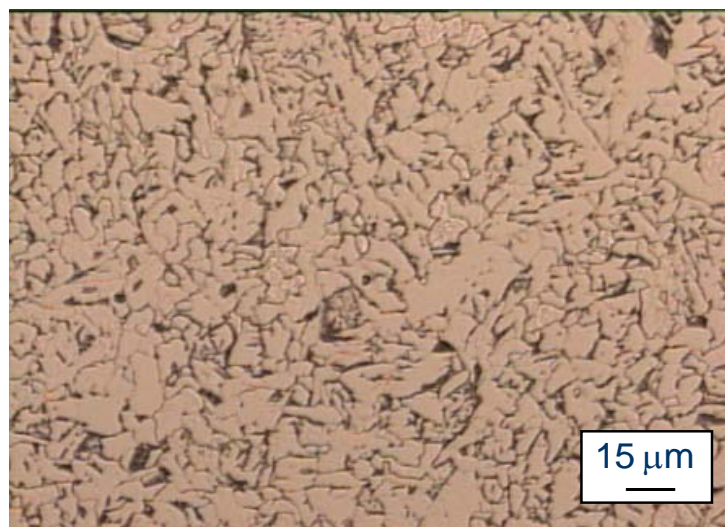


Figure 31 Optical micrograph of the ferrite microstructure in 272244 csp4, prepared using 3% Nital solution

Table 14 below shows the chemical composition of 7631 and Table 14 shows the results from the optical microstructural analysis made.

Table 13 Chemical composition of 7631

Grade	C	Si	Mn	S	P	Al	Nb	V	Ti	B
7631	0.180	0.03	0.67	0.008	0.008	0.035	-	-	0.019	-

Table 14 Results from the microstructural analysis of 7631 hot band materials

Coil ID Info	272244 CSP4	272244 CP5
Grade	7631	7631
Average Grain Size(μm)	6.15	6.35
% Ferrite	87.2	84.2
Hardness	149.1	139.3
Std Dev	3.3	3.9

Under the high magnifications of the SEM the secondary phase appears to be mainly pearlitic in structure and well distributed throughout the bulk.

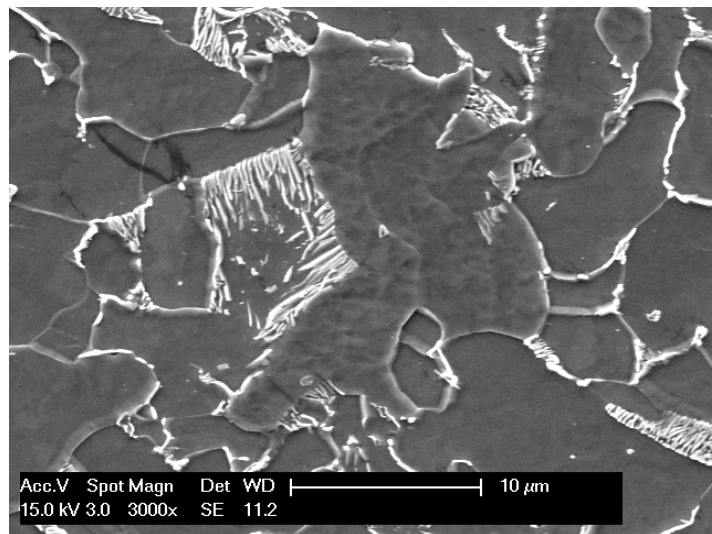


Figure 32 Secondary electron SEM micrograph showing the microstructure as well as the nature of the secondary phase in the 272244 csp4 hot band material.

Using the electron backscatter diffraction method, the IQ data collected shows a 3 peak distribution very similar to that of 7045 with polygonal and acicular ferrite peaks. However in this case the third peak is more distinct and represents the presence of pearlite.

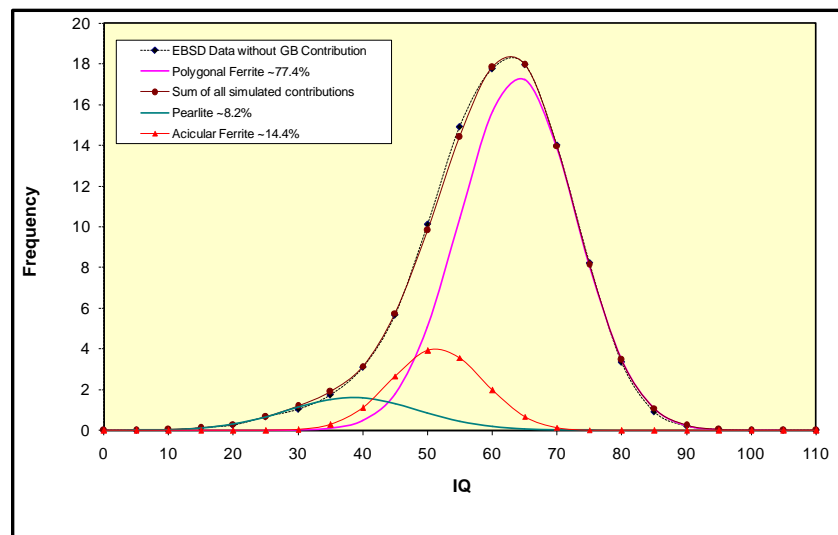


Figure 33 EBSD-IQ distribution curve for 7631 Hot band material showing peaks for each phase identified

Using the data from the EBSD-IQ as well as the information gathered using the microscopy methods a total micro-constituent phase balance was constructed, this phase balance is shown in the table below.

Table 15 Results from EBSD-IQ analysis of 7631 hot band material

Steel Grade	α (Polygonal Vol.%)	α (Acicular Vol.%)	Pearlite (Vol.%)	High Carbon Constituents (Vol.%)
7631	77.4	14.4	8.2	-

5.2 TRANSFORMATION STUDY

Using the hot band material samples were prepared and subject to continuous cooling dilatometry experiments in order to understand the nature of the transformations in the steels used in this investigation. As a reference the PC software J-Mat Pro was used to calculate the continuous cooling transformations for each of the different alloys and used to aid in the analysis of the dilatometer results. For all cooling tests csp4 samples were used.

After each cooling experiment both optical and scanning electron micrographs of each sample were taken. These micrographs were then used in conjunction with the J-Mat Pro analysis as well as the dilatometric readings to develop an experimental CCT for the hot band material received.

5.2.1 Continuous Cooling of 7045

Figure 34 shows the J-Mat Pro results of a CCT simulation for 7045. The results show a ferrite transition between 750 and 850 °C depending on the cooling rate, with the bainitic and pearlitic starting temperatures happening at least 150 °C lower.

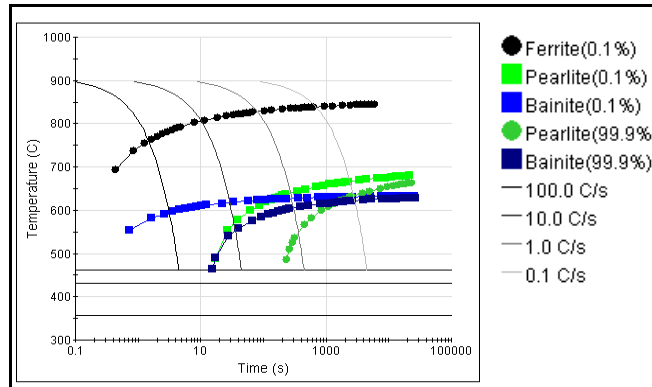


Figure 34 Continuous cooling transformation diagram produced by J-Mat Pro for 7045

After running the computer simulations for 7045, the actual continuous cooling experiments were run with the resulting microstructures shown in figure 35. In the figure the microstructures are shown in comparison to each other as well as the microstructure of the as received hot band. In every case the ferrite grain size resulting from the dilatometry experiments is larger than that observed in the as-received hot band condition. In addition as expected as the cooling rate increases the nature of the ferrite seems to change from polygonal to non-polygonal ferrite and the second phase seems to be a mixture of pearlite and low temperature transformation product, i.e. bainite.

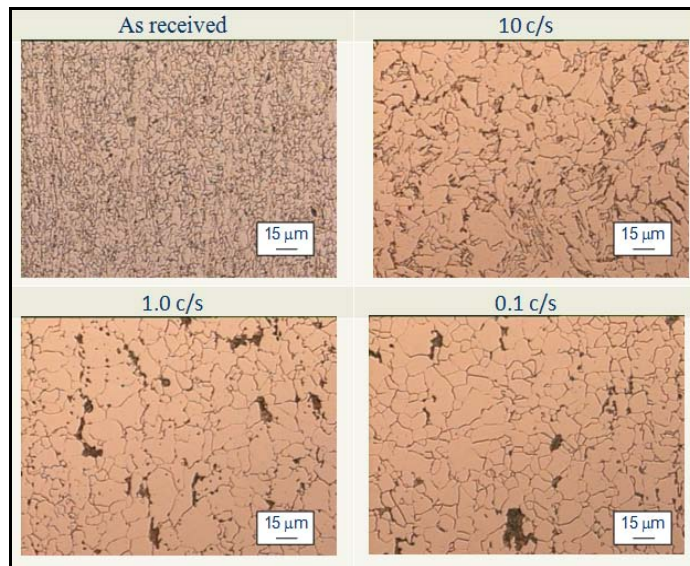


Figure 35 Optical micrographs of each cooling experiment and the as received hot band material for 7045.

With the aid of the SEM the nature of the secondary phase is revealed in each of the cooling conditions. At the higher cooling rates there is some pearlite but most of the secondary phase is just segregated high carbon particles, like bainite. In both 1.0 and 0.1 C/s conditions the secondary phase forms as pearlite, with little, if any other phases present.

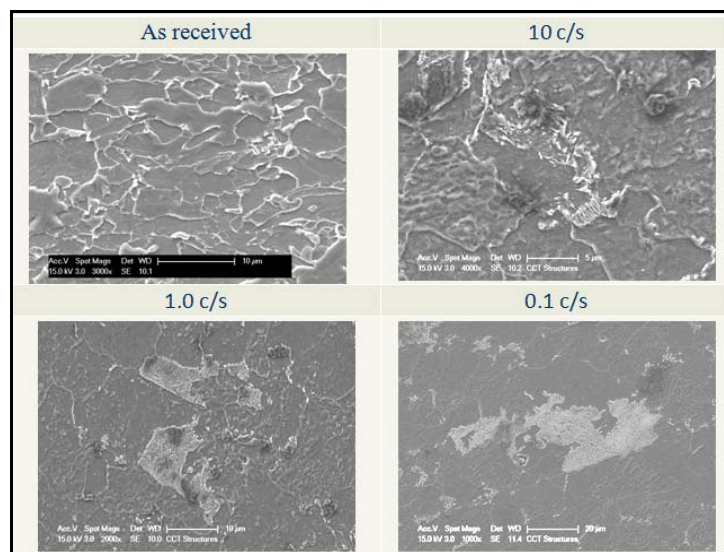


Figure 36 Electron micrographs of each cooling experiment and the as received hot band material for 7045.

5.2.2 Continuous Cooling of 7153

The CCT diagram for 7153 as determined by J-Mat Pro in figure 37 shows that each of the transformations is occurring at separate temperatures with very little overlap in the transformations.

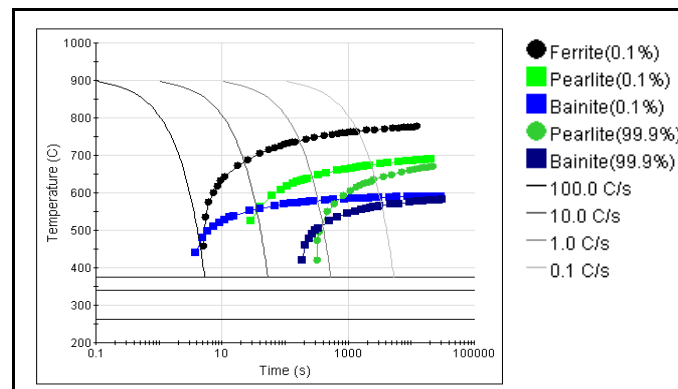


Figure 37 Continuous cooling transformation diagram produced by J-Mat Pro for 7153

Again, in the figure below the comparison of the final microstructures of each continuously cooled sample is compared to the as received microstructure. In the case of 7153 the higher cooling rates lead to significantly different microstructures, with very little ferrite. Conversely, the lower 0.1 C/s cooling rate shows a microstructure almost identical to the hot band material.

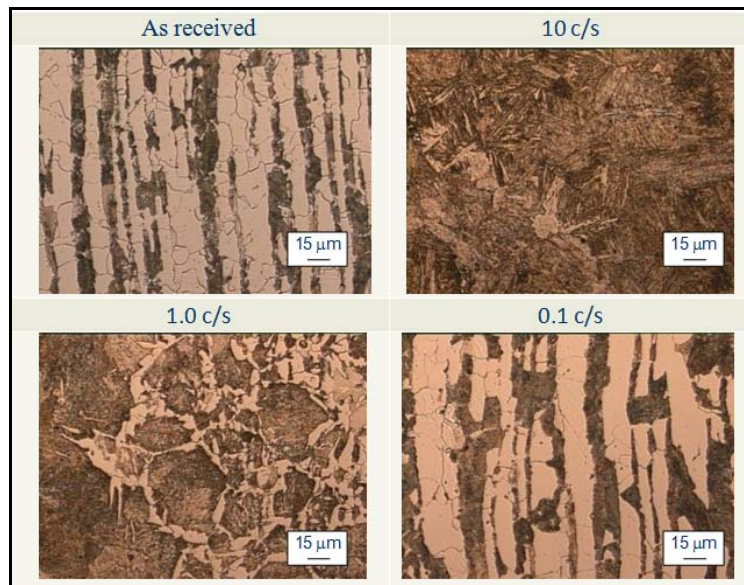


Figure 38 Optical micrographs of each cooling experiment and the as received hot band material for 7153

Next, the microstructures were examined under the SEM showing the microstructure for the 10 C/s condition is primarily bainitic as predicted by the theoretical CCT diagram. At 1.0 C/s condition we have a mixture of bainite, acicular ferrite and pro-eutectoid ferrite nucleated at the prior austenite grain boundaries. At the very low cooling rates, 0.1 C/s, the resulting microstructure is banded and very similar to the one observed in the hot band condition.

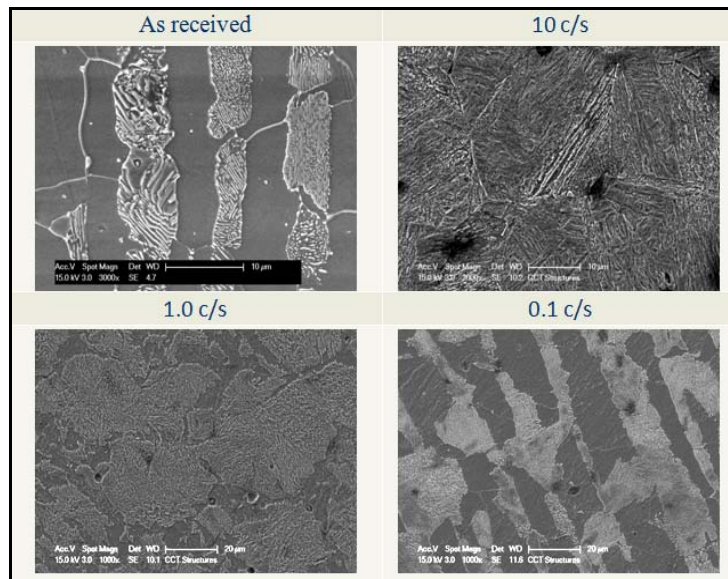


Figure 39 Electron micrographs of each cooling experiment and the as received hot band material for 7153

5.2.3 Continuous Cooling of 7038

The CCT from the J-Mat Pro calculations shows very little separation between the ferrite and pearlite transition, with the bainite transition coming into play at much lower temperatures. The figure below is the output from the software simulation.

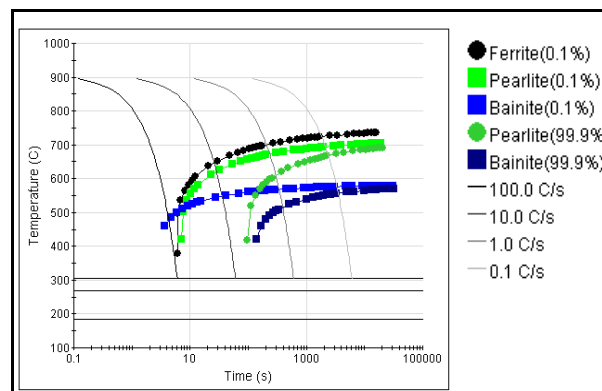


Figure 40 Continuous cooling transformation diagram produced by J-Mat Pro for 7038

In the optical micrographs of 7038 cooling comparisons, the 10 C/s sample showed some non-polygonal ferrite with indications of bainitic constituents and little, if any, pearlite. For the lower cooling rates (1.0 and 0.1 C/s) the amount polygonal ferrite increases significantly and the secondary phase appears to be more predominantly pearlitic in nature. Again the ferrite grain size in the continuously cooled samples is much larger than that of the as received structure.

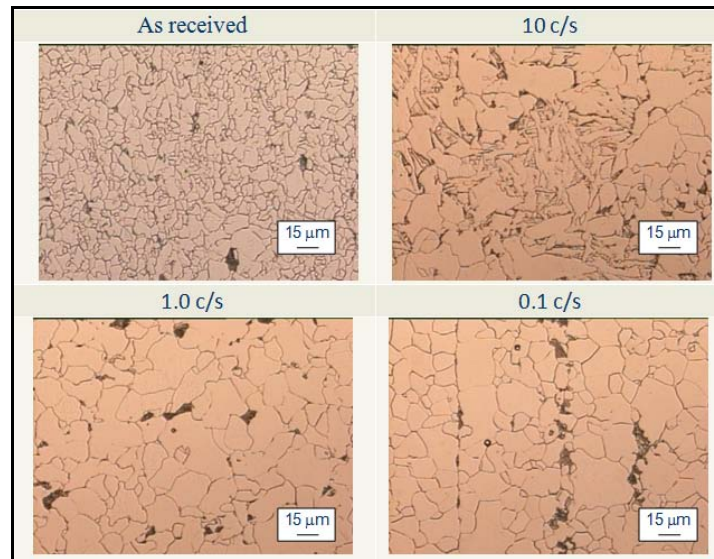


Figure 41 Optical micrographs of each cooling experiment and the as received hot band material for 7038

The observations made with the higher magnifications of the SEM verify those made optically showing that and 1.0 C/s cooling rate results in a microstructures most similar to that found in the hot band.

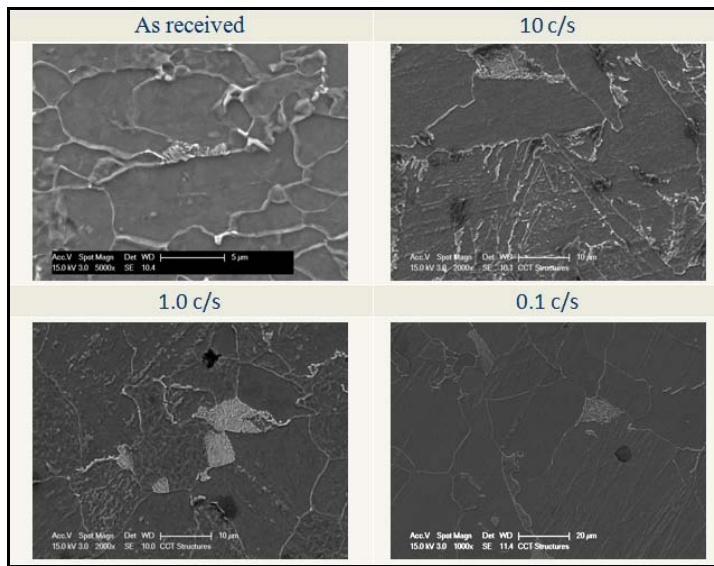


Figure 42 Electron micrographs of each cooling experiment and the as received hot band material for 7038

5.2.4 Continuous Cooling of 7631

In the CCT diagram for 7631, the computer simulation software shows that the transition temperature during cooling is significantly different for each of the expected phases.

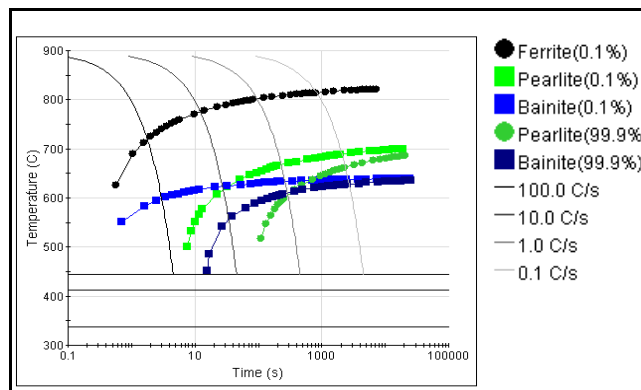


Figure 43 Continuous cooling transformation diagram produced by J-Mat Pro for 7631

From the micrographs in the figure below significantly different microstructures are once again evident for each cooling condition. In the 0.1 C/s condition a somewhat banded structure with large polygonal grains and large secondary phase colonies are present. When the cooling rate is increased to 1.0 C/s the banding begins to be disrupted by acicular ferrite formation, similar to the structure found in the hot band, and the secondary phase colonies are smaller. Finally, in the 10 C/s condition the structure appears to have very elongated acicular ferrite grains interspersed with thin secondary phase colonies. Also, in these experiments the ferrite grain structure exhibited is always much larger than that of the hot band.

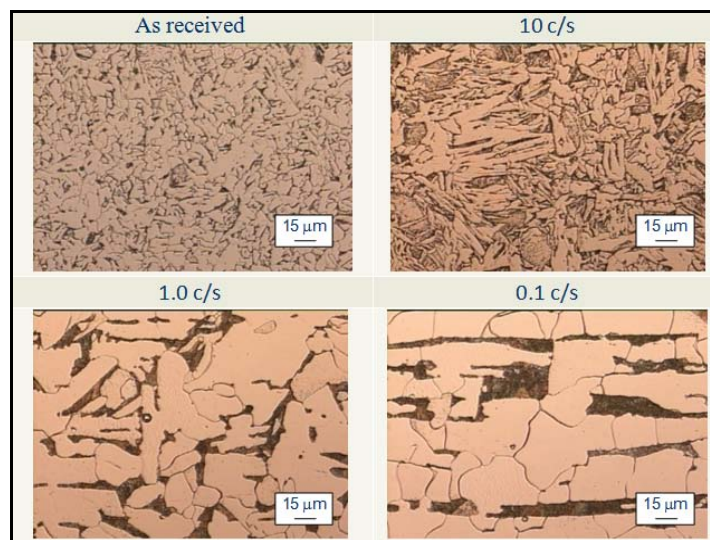


Figure 44 Optical micrographs of each cooling experiment and the as received hot band material for 7631

Under the electron microscope the characteristics of the secondary phases become apparent. In the 1.0 and 0.1 C/s conditions, pearlite is the only secondary phase found. Meanwhile, with the high cooling rate condition a mix of pearlite and bainitic structures are evident in the micrographs.

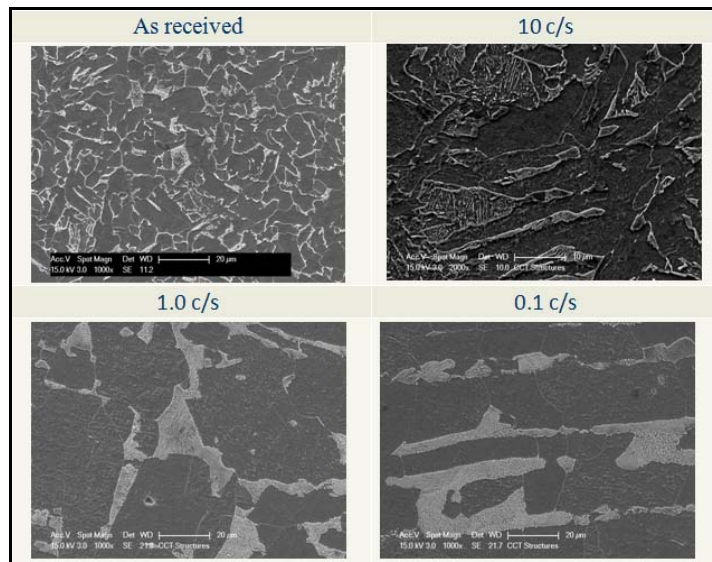


Figure 45 Optical micrographs of each cooling experiment and the as received hot band material for 7631

Through these cooling experiments a good comparison was made between the resulting microstructures formed through the different cooling rates. For each alloy, the cooling condition which resulted in a final microstructure most similar to that of the hot band was closely analyzed and used to help determine the condition for the thermomechanical processing experiments.

5.3 THERMOMECHANICAL PROCESSING

Using the computer controlled high temperature MTS compression testing system, hot rolling experiments were designed and carried out. Cooling rates of 10 and 30 C/s from the final rolling temperatures to the coiling temperatures were used. The MTS compression machine records force-displacement-time data this is then taken and converted in the true-stress vs. true strain and analyzed.

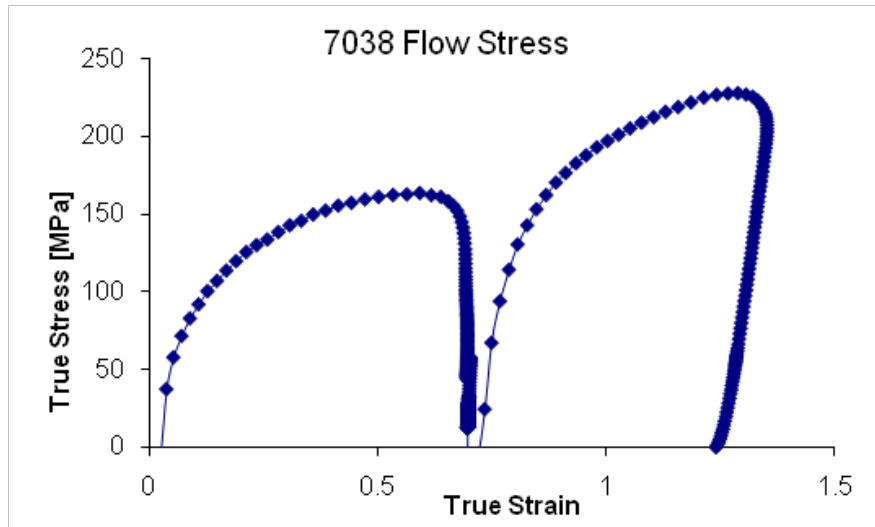


Figure 46 Example flow stress plot from data taken during compression test on the MTS machine

The plot in figure 46 shows the data taken from one of the compression tests run. The first curve is the flow stress at the high temperature of deformation, while the second curve is the flow stress of the second deformation at the lower temperatures. These results were analyzed and the peak stress at each temperature was extracted. The same procedure was done for all the steels investigated in this study, Table 16 shows the results of the peak stress for each steel samples and deformation conditions.

Table 16 Average peak deformation stress of each alloy during compression testing. 7038 has two values for the second rolling temperature since two different conditions were used.

Grade	True Stress at T_{rolling1} (MPa)	True Stress at T_{rolling2} (MPa)
7045	169	209
7153	190	233
7631	187	257
7038	165	219/286

After the final deformation of TMP was carried out, at the finishing temperature, the samples were cooled at 10 or 30 C/s at the prescribed coiling temperature. The samples fully processed were then analyzed using the same optical microscopy methods as the hot band materials. The sections below show the results of this analysis. In the process of these analyses, microhardness values were measured for each of these samples, these results are also included.

5.3.1 Thermomechanical Processing of 7045

Figure 47 below shows how the cooling procedure after hot rolling, which was used in the TMP simulations, compares to the continuous cooling transformations diagram for the 7045 grade tested.

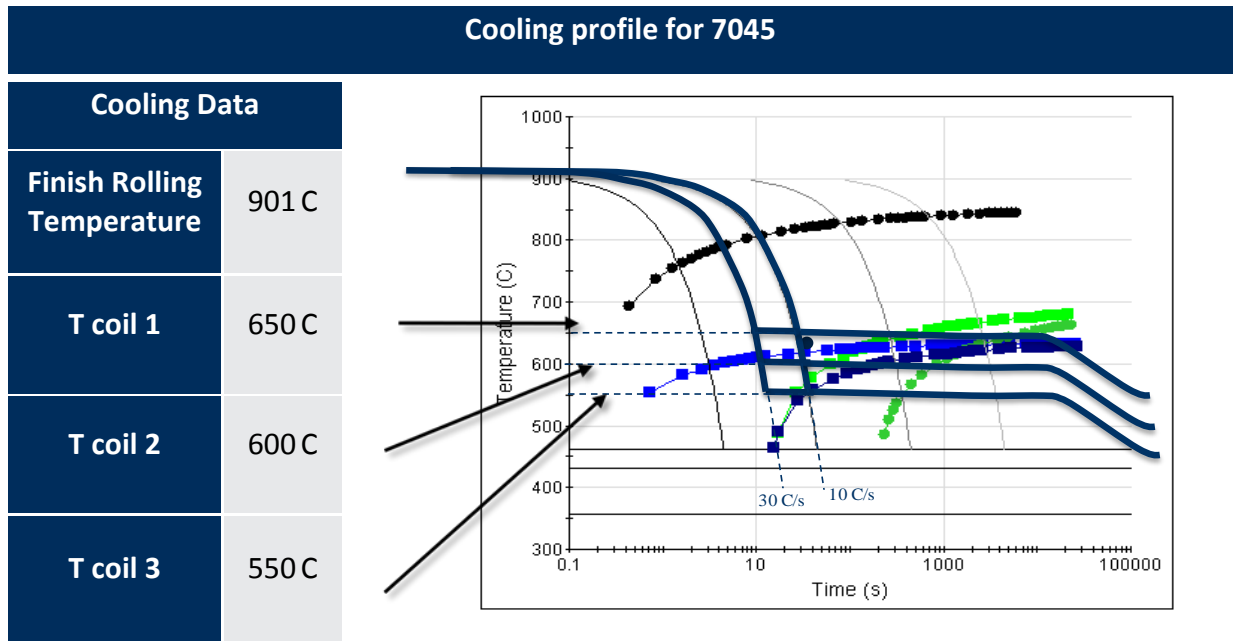


Figure 47 Schematic of the processing temperatures in comparison to the transformation diagram for 7045

The following figures show the final microstructures which evolved from each of the TMP tests which were run.

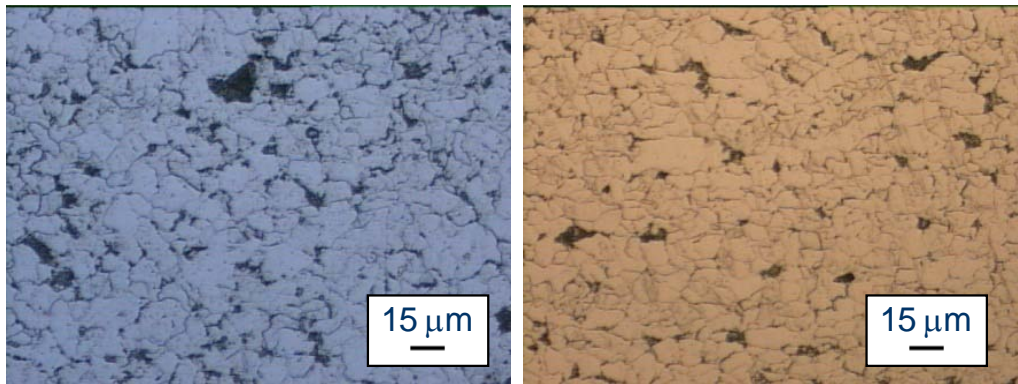


Figure 48 Microstructure resulting from TMP processing of 7045 with $T_{\text{coil}} = 650$,
Left (10 c/s to coiling), Right (30 c/s to coiling)

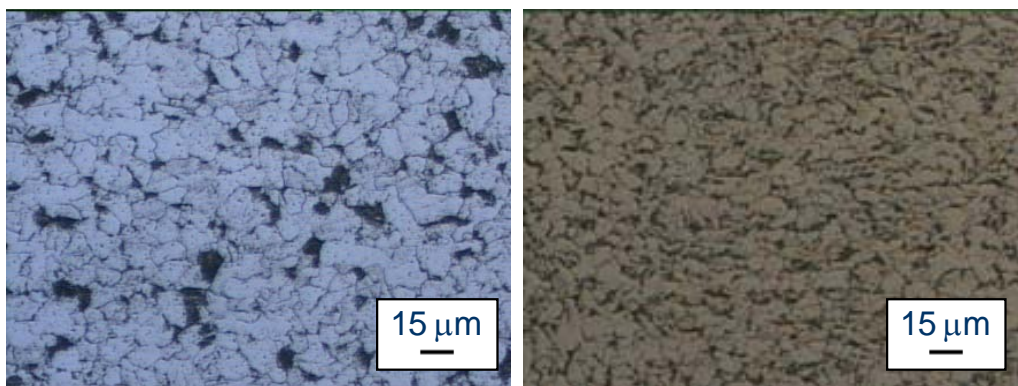


Figure 49 Microstructure resulting from TMP processing of 7045 with $T_{\text{coil}} = 600$,
Left (10 c/s to coiling), Right (30 c/s to coiling)

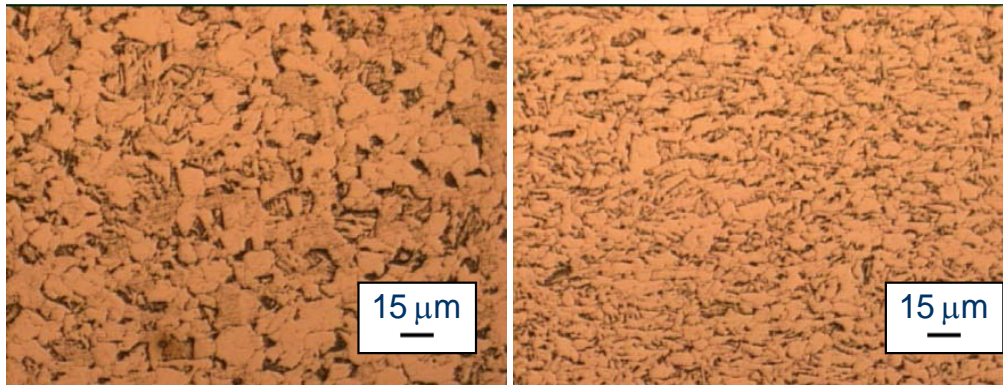


Figure 50 Microstructure resulting from TMP processing of 7045 with $T_{\text{coil}} = 550$,
Left (10 c/s to coiling), Right (30 c/s to coiling)

An analysis of each processing condition was made with the results of which are in table 17 below.

Table 17 Results from the microstructural analysis of the TMP simulation,
including microhardness, for 7045

Steel Grade	7045	7045	7045	7045	7045	7045
T_{coil}	550	600	650	550	600	650
Cooling Rate (C/s)	10	10	10	30	30	30
Grain Size (μm)	8.68	11.69	9.35	5.02	5.5	7.77
% Ferrite	88	92.4	90.5	93.5	91.5	93.3
VHN	186.8	179.2	173.4	185.2	182.7	151

For this grade, the cooling rate has the most effect on the microstructure. In all cases the 30 C/s cooling conditions lead to much smaller grain sizes. Also, in the case of the coiling temperature of 550 °C, the nature of the microstructure changes to where some acicular ferrite has formed and not all of the secondary phase appears to be pearlite.

5.3.2 Thermomechanical Processing of 7153

As a tool for analysis, the CCT diagram for 7153, from the J-Mat Pro computer simulations, were overlaid with the processing parameters which were to be used in the tests.

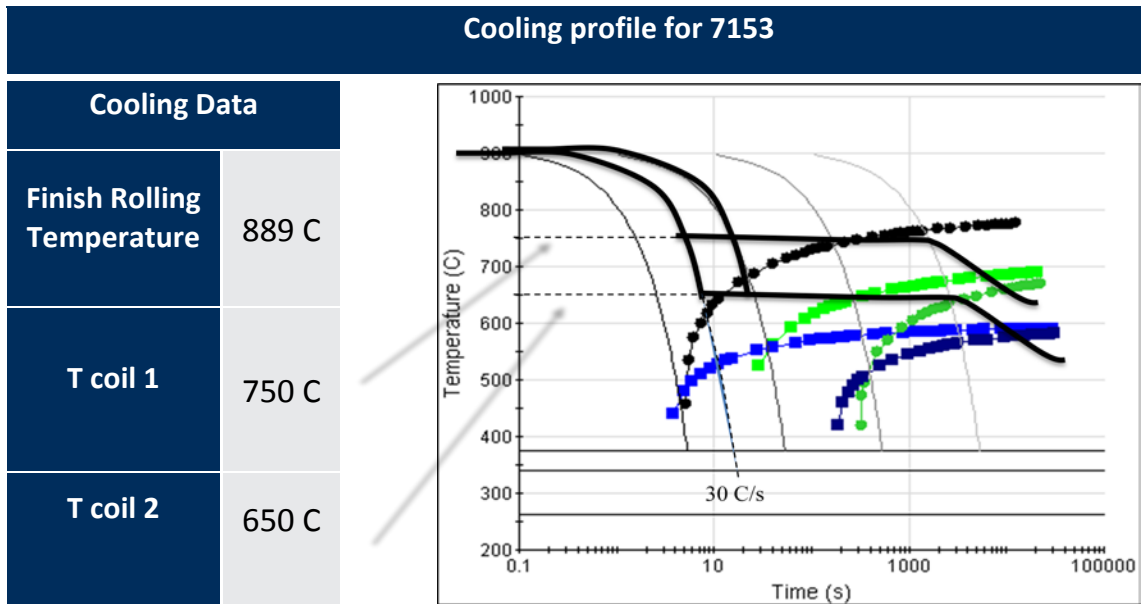
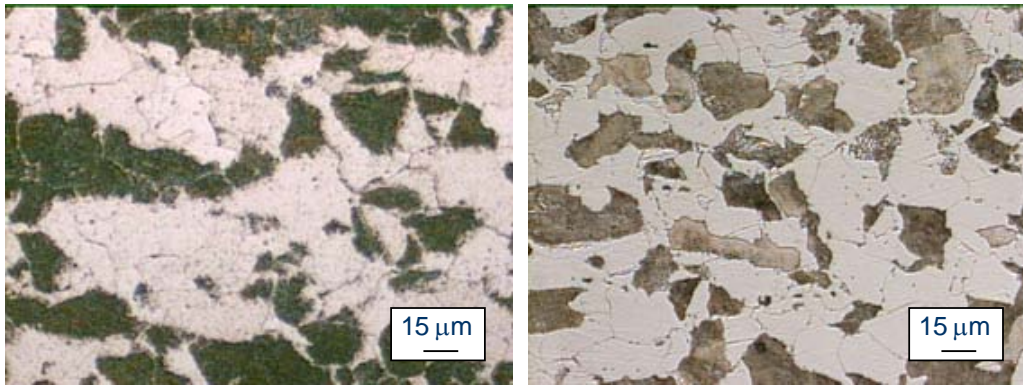
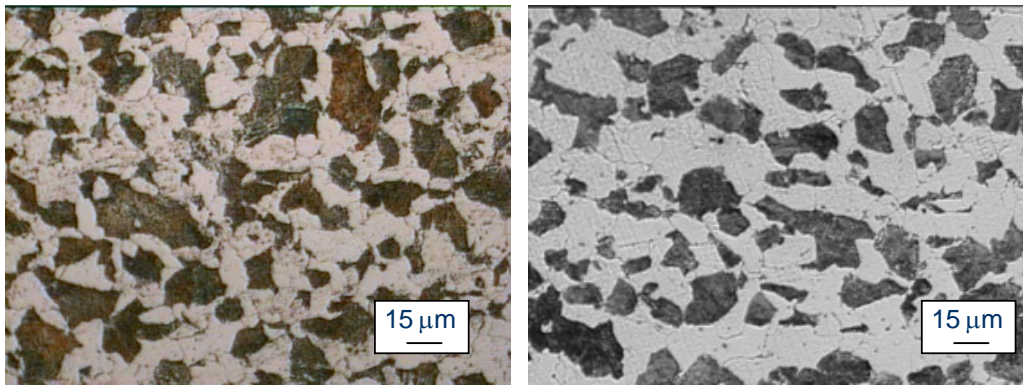


Figure 51 Schematic of the processing temperatures in comparison to the transformation diagram for 7153

After each run was completed the microstructure of the final product was revealed and micrographs taken, some example micrographs are shown in the figures below.



**Figure 52 Microstructure resulting from TMP processing of 7153 with $T_{\text{coil}} = 750$,
Left (10 c/s to coiling), Right (30 c/s to coiling)**



**Figure 53 Microstructure resulting from TMP processing of 7153 with $T_{\text{coil}} = 650$,
Left (10 c/s to coiling), Right (30 c/s to coiling)**

After the TMP simulations were run and microstructures revealed each sample was analyzed using the standard characterization techniques described earlier. The Table below shows these results

Table 18 Results from the microstructural analysis of the TMP simulation, including microhardness, for 7153

Steel Grade	7153	7153	7153	7153
Tcoil	650	750	650	750
Cooling Rate (C/s)	10	10	30	30
Grain Size (μm)	9.87	10.01	9.06	9.94
% Ferrite	57.1	62.8	65.5	63.6
VHN	188.1	187	210.5	191.1

In all cases, compared to the hot band material significantly less banding was evident, and the higher cooling rate show even less banding than the lower cooling rates. The cooling rate appears to have little effect on the overall grain size. For 7153 coiling temperature appears to be the biggest factor in both grain size and morphology of the secondary phase. The specimens which were cooled to 750 °C show a larger grain size than those cooled to 650 °C. The micrographs also show that the sample cooled to 750 at 10 C/s shows the most significant banding structure.

5.3.3 Thermomechanical Processing of 7631

The diagram below shows the cooling conditions used in the 7153 TMP simulation runs overlaid on the CCT generated by J-Mat pro.

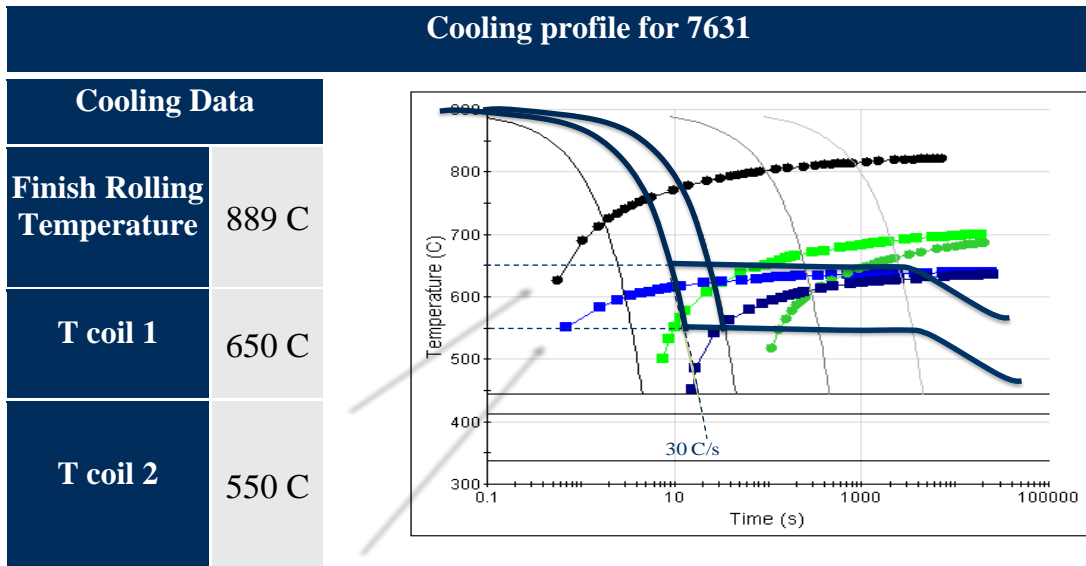


Figure 54 Schematic of the processing temperatures in comparison to the transformation diagram for 7631

The figures below are micrographs of the microstructures revealed after each run was completed.

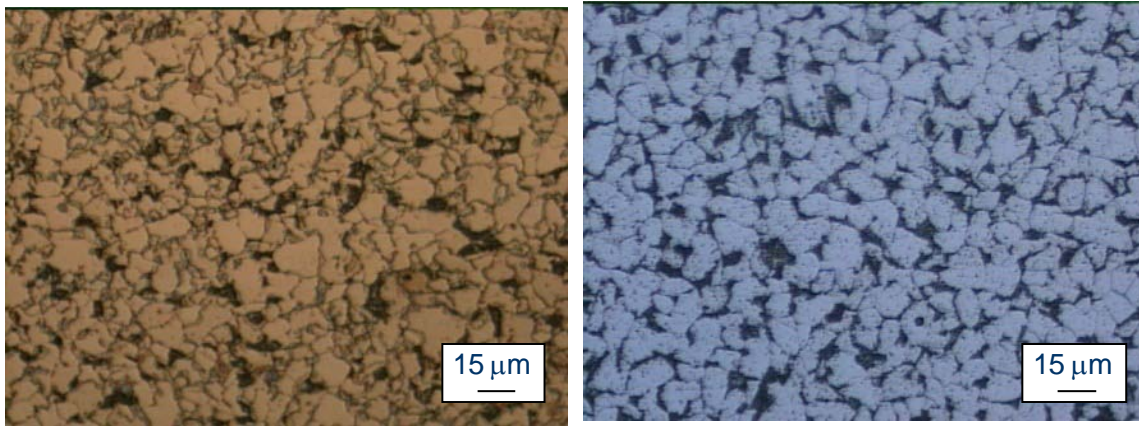


Figure 55 Microstructure resulting from TMP processing of 7631 with $T_{coil} = 650$,
Left (10 c/s to coiling), Right (30 c/s to coiling)

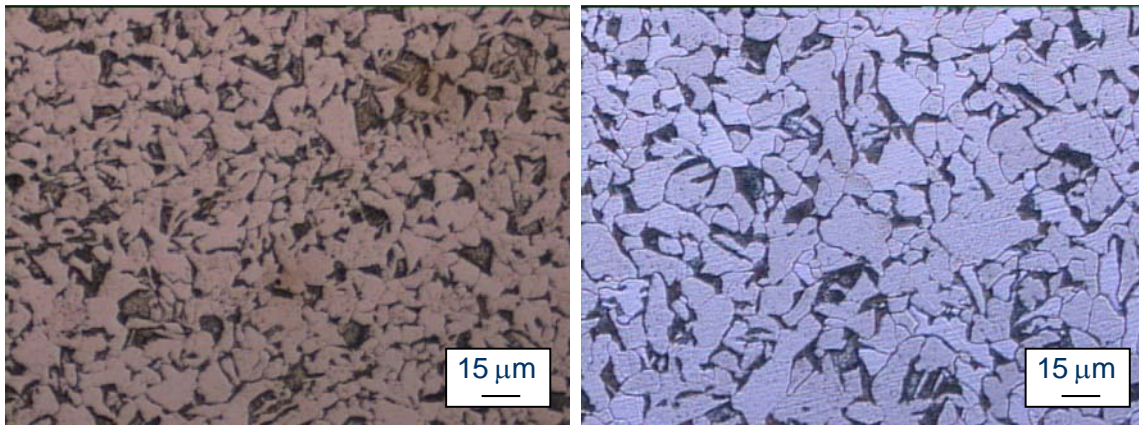


Figure 56 Microstructure resulting from TMP processing of 7631 with $T_{coil} = 550$,
Left (10 c/s to coiling), Right (30 c/s to coiling)

After the TMP simulations were run and microstructures revealed each sample was analyzed using the standard characterization techniques described earlier. The Table below shows these result.

Table 19 Results of the microstructural analysis of the TMP simulation, including microhardness, for 7631

Steel Grade	7631	7631	7631	7631
Tcoil	550	650	550	650
Cooling Rate (C/s)	10	10	30	30
Grain Size (μm)	9.88	9.2	7.61	7.44
% Ferrite	82.8	85.6	80.4	88.5
VHN	142.9	136.6	146.3	168.5

The results from the TMP experiments for 7631 show that the cooling rate has a major effect on refining the final ferrite grain size. Also, the lower coiling temperature resulted in a much different grain morphology. The samples cooled to 550 °C have a structure that appears to have some acicular ferrite, as well as some secondary phases which are bainitic in nature. The coiling temperature did not, however, seem to greatly impact the grain size in both cases.

5.3.4 Thermomechanical Processing of 7038

Finally the TMP simulations of 7038 were carried out. The schematic below shows the cooling conditions for this grade overlaid on the CCT diagram from J-Mat Pro. For 7038, two separate final rolling temperatures were used, creating a total of 8 conditions.

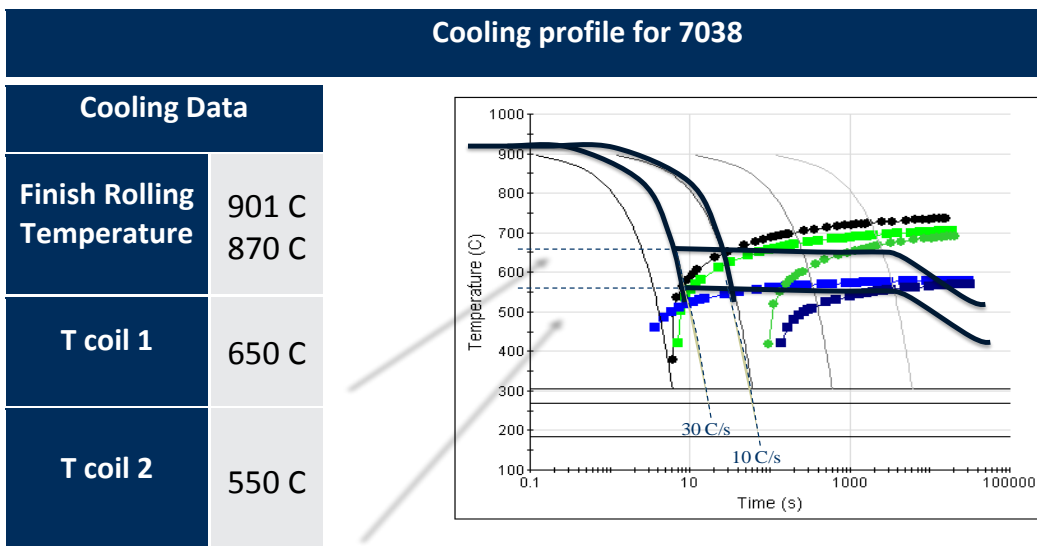


Figure 57 Schematic of the processing temperatures in comparison to the transformation diagram for 7153, only 1 finish rolling temperature is shown for simplicity.

The microstructures for each of the eight runs are shown in the micrographs below. In these sets of figures the microstructures of the samples with the same cooling rate and coiling temperature are arranged with each other, so that it is the final rolling temperature that differentiates the pair of images. The first four images are from the 10 C/s cooling processes.

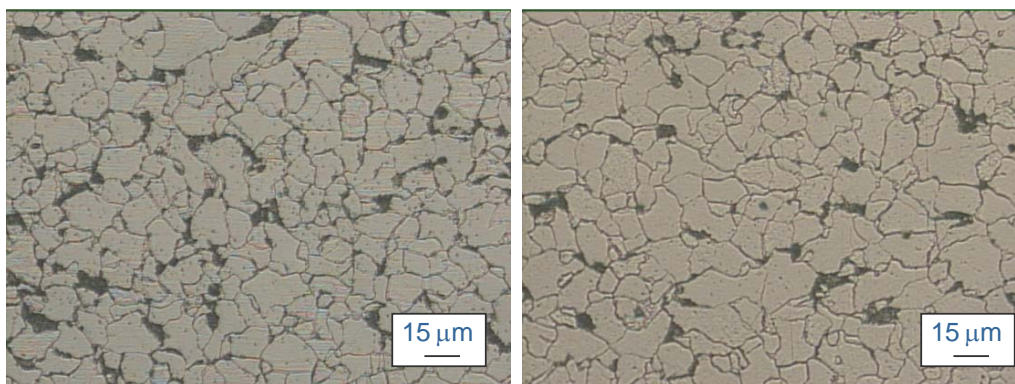


Figure 58 Microstructure resulting from TMP processing of 7038 with $T_{\text{coil}} = 650$ @ 10 C/s Cooling, Left ($T_{\text{finish}} = 901$), Right ($T_{\text{finish}} = 870$).

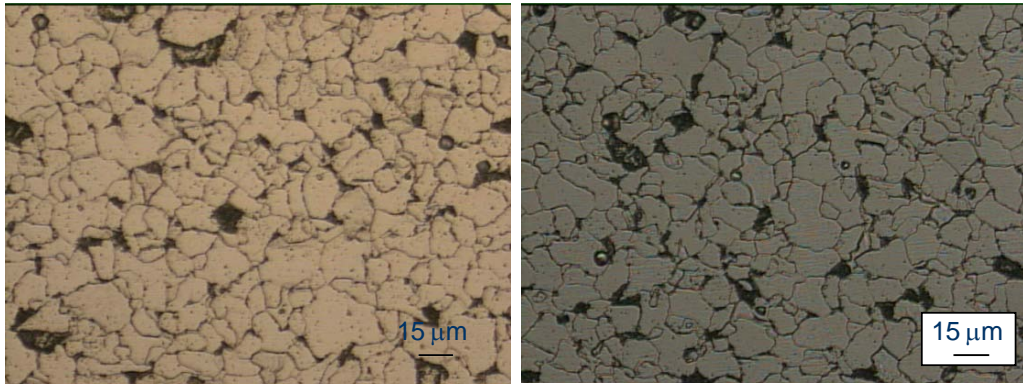


Figure 59 Microstructure resulting from TMP processing of 7038 with $T_{\text{coil}} = 550$ @ 10 C/s Cooling, Left ($T_{\text{finish}} = 901$), Right ($T_{\text{finish}} = 870$).

Following the micrographs of the 10 C/s samples are micrographs from the 30 C/s TMP simulations.

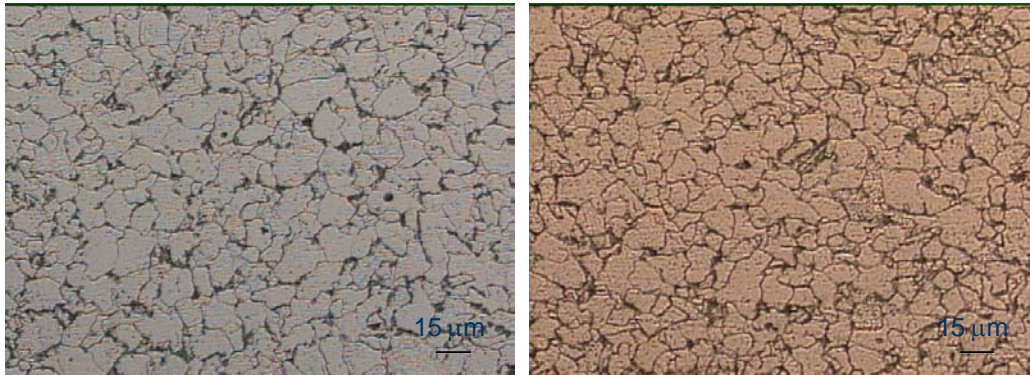


Figure 60 Microstructure resulting from TMP processing of 7038 with $T_{\text{coil}} = 650$ @ 30 C/s Cooling, Left ($T_{\text{finish}} = 901$), Right ($T_{\text{finish}} = 870$).

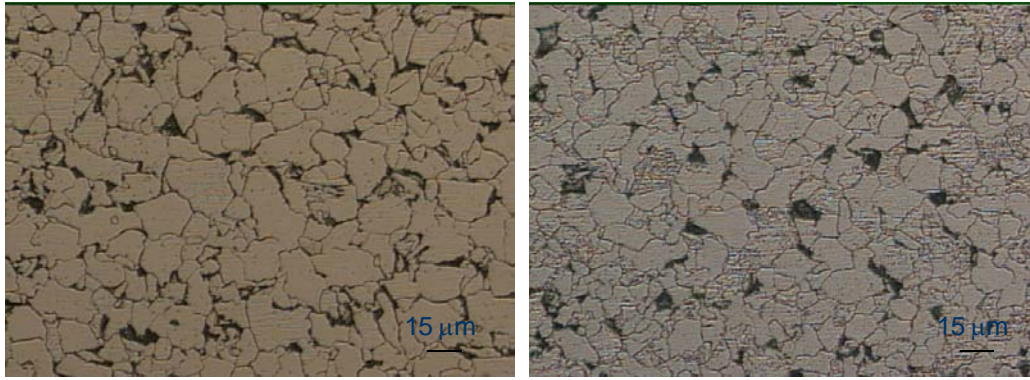


Figure 61 Microstructure resulting from TMP processing of 7038 with $T_{coil} = 550$ @ 30 C/s Cooling, Left ($T_{finish} = 901$), Right ($T_{finish} = 870$).

Tables 20 and 21 below have the results from the analysis performed on the processed samples. Table 20 are the results from the high rolling temperature of 901 °C, and table 21 has the results from the low finish rolling temperature of 870 °C.

Table 20 Results from the microstructural analysis of the TMP simulation, including microhardness, for 7038 with a finish rolling temperature of 901 °C

Steel Grade	7038	7038	7038	7038
Tcoil	550	650	550	650
Cooling Rate (C/s)	10	10	30	30
Grain Size (μm)	9.65	9.57	7.99	8.45
% Ferrite	84.55	90.42	88.08	92.83
VHN	135.4	129.9	136.8	146.7

Table 21 Results from the microstructural analysis of the TMP simulation, including microhardness, for 7038 with a finish rolling temperature of 870 °C

Steel Grade	7038	7038	7038	7038
Tcoil	550	650	550	650
Cooling Rate (C/s)	10	10	30	30
Grain Size (μm)	9.77	10.34	7.42	8.38
% Ferrite	89.53	93.77	94.34	93.26
VHN	125.1	127.6	138.1	131.6

First, for 7038, the two separate finishing temperatures appear to have little overall effect on the final microstructure and morphology of the grain in each case. However, at the lower finishing temperature the effect of coiling temperature appears to be more pronounced. With the final rolling temperature of 901 °C and a cooling rate of 10 C/s the difference in grain size between the samples with varying coiling temperature is very small, less than 0.1 μm, and with the lower finishing temperature this difference is on the order of 0.5 μm. Also, in all cases, the cooling rate appears to have a significant effect on grain size, with the faster cooling rates yielding a smaller ferrite grain size. Finally, the lower finishing temperature always leads to more ferrite in the phase balance. This difference in the amount of ferrite can be rather significant.

6.0 DISCUSSION

6.1 EFFECT OF SKIN PASS IN HOT BAND MATERIAL

During the characterization of the hot band materials, microhardness measurements showed some unexpected results in the samples of 7038 received. The chart below shows the differences in the hardness values measured in the samples of hot-band material received for 7038.

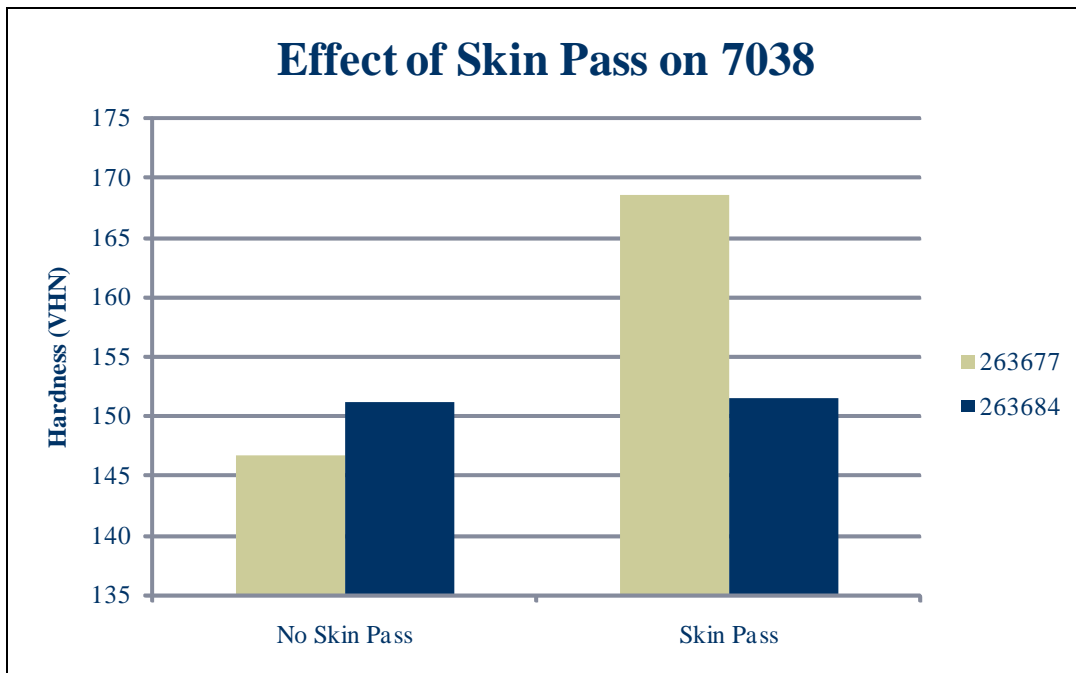


Figure 62 Graph showing effect of the skin pass on two samples of alloy 7038.

The chart above shows the results of hardness test and how the skin pass process affects the hardness response of the samples given. In this particular case it would seem that the P content between sample 263677(0.0137 P wt%) compared to sample 263684 (0.0088 P wt%) is responsible for the increase in hardness. The effect of temper rolling or small deformations on increasing the YS through grain boundary hardening due to P segregation is well-known.^{40, 41\}

6.2 PREDICTED YIELD STRESS OF THE HOT BAND MATERIAL

Upon completion of the hot-band characterization an extended Hall-Petch equation was used in order to predict the yield stress in the steels investigated

$$\sigma_{ys} = \sigma_{pn} + \sigma_{ss(c)} + \sigma_{ss(Si)} + \sigma_{ss(Mn)} + k_y(d^{-1/2}) \quad (7)$$

$$\sigma_{pn} = 88 \text{ MPa}$$

$$k_y = 18.1$$

$$\Delta \sigma_{ss(C)} = 4.57 * (\%C)$$

$$\Delta \sigma_{ss(Si)} = 84 * (\%Si)$$

$$\Delta \sigma_{ss(Mn)} = 37 * (\%Mn)$$

(8-12)

The equation above takes into account the effects of solid solution of C, Si, and Mn as well as the grain size strengthening effect with a Hall-Petch parameter of $k_y = 18.1$.

The resulting values are shown in the table below.

Table 22 Predicted yield stress (PYS) in MPa calculated for each hot band sample investigated

	244CSP4 (7631)	244CP5 (7631)	655CSP1 (7045)	655CSP4 (7045)	174CSP1 (7153)	174CSP4 (7153)	677CSP4 (7038)	677CP5 (7038)	684CSP4 (7038)	684CP5 (7038)
PYS (MPa)	305.46	293.17	416.18	406.99	313.40	309.01	346.90	344.35	349.99	333.27

After completing the calculations for predicted yield stress these numbers were compared to yield stress values measured in the commercial hot band material. In these cases the value provided correspond well with the values calculated using the extended Hall-Petch model.

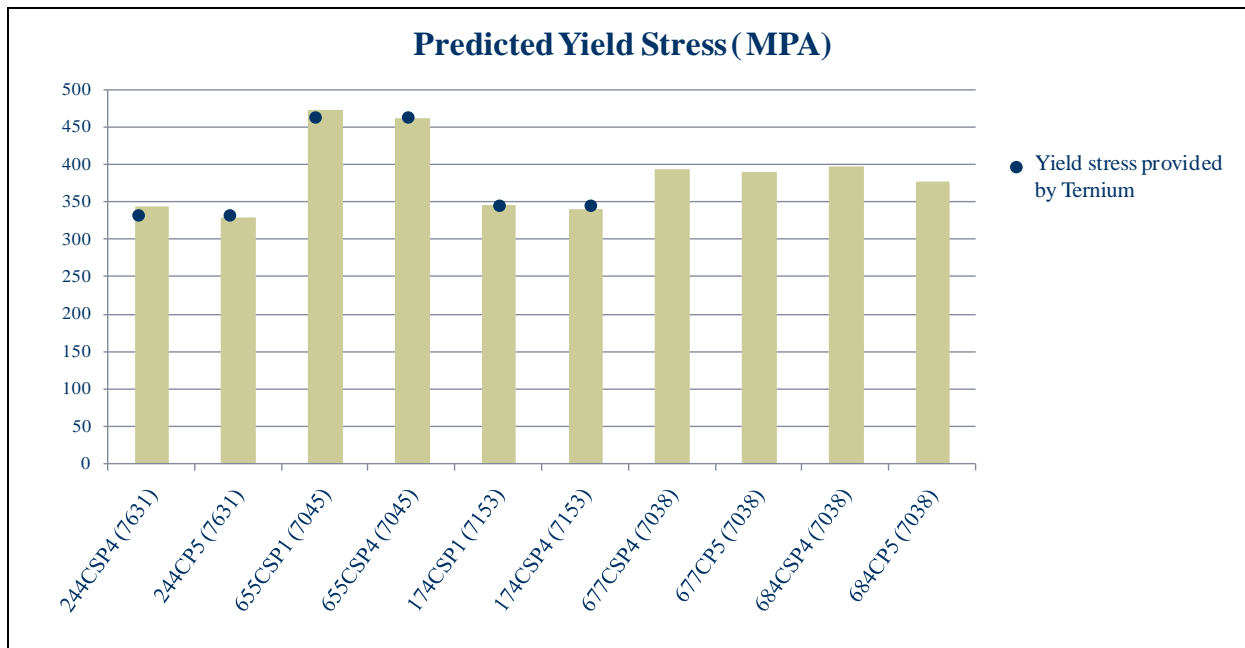


Figure 63 Chart showing the predicted yield stresses according to Hall-Petch model with dark plot points showing yield stress values measured.

The additional implications of the results presented in Figure 62 also seem to indicate that any strengthening due to precipitation or dislocation is minimal.

6.3 TRANSFORMATION STUDY

Using the results from the dilatometry experiments, as well as the micrographs and J-Mat Pro predictions of continuous cooling transformations an experimental CCT diagram was constructed for each alloy in the hot band. These would differ from those calculated by the computer model due to differences in characteristics of the austenite (composition and grain size) prior to transformation. J-Mat Pro uses an ideal, fully recrystallized, austenite grain structure of a given size; on the other hand the hot band material used in the dilatometry experiments were reheated to the final rolling temperature and then cooled again, in this case very little grain growth if any takes place. Due to these factors the kinetics of the transformations are much more similar to those of the transformations after rolling during the thermomechanical processing of these steels. The following four figures show the transformation temperatures determined from the dilatometric experiments.

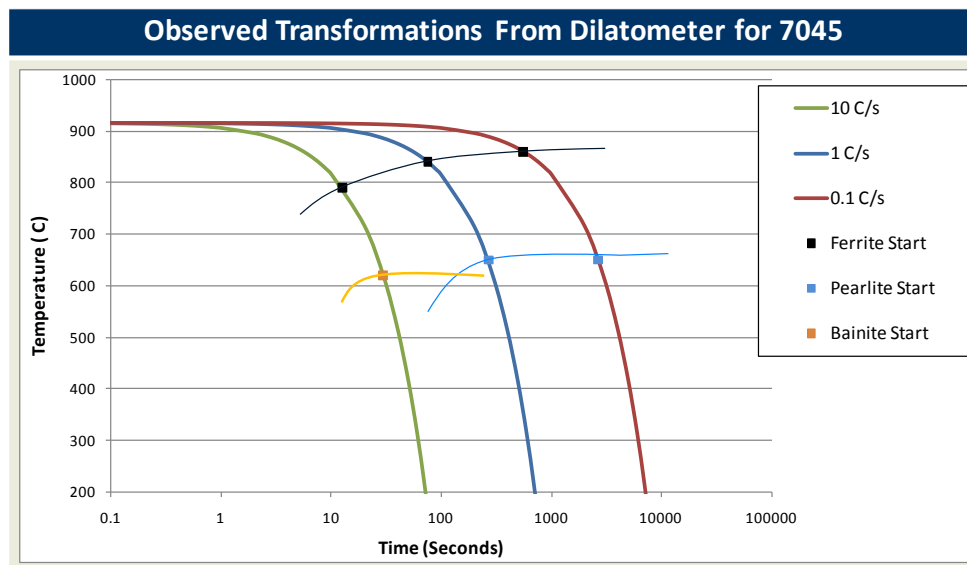


Figure 64 Continuous Cooling Diagram showing the transformation temperatures observed in the cooling experiments for 7045

Observed Transformations From Dilatometer for 7153

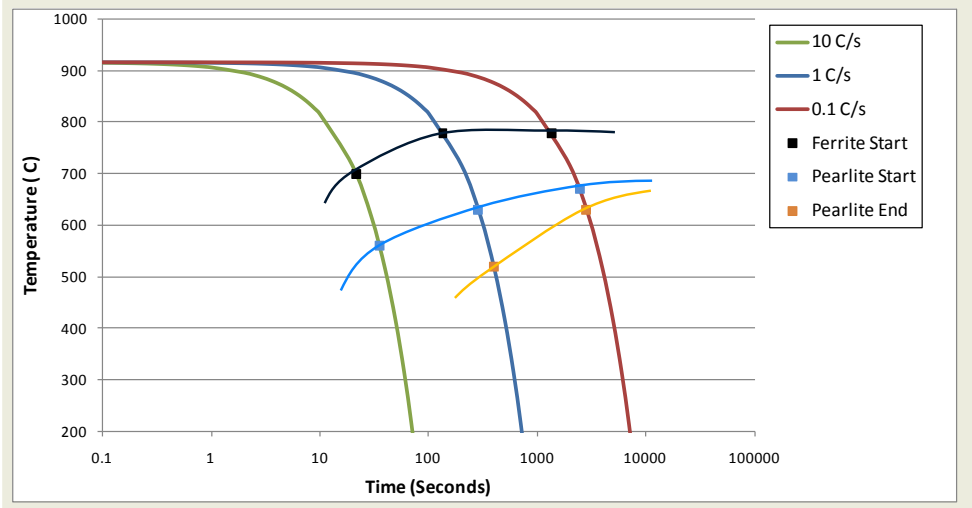


Figure 65 Continuous Cooling Diagram showing the transformation temperatures observed in the cooling experiments for 7153

Observed Transformations From Dilatometer for 7631

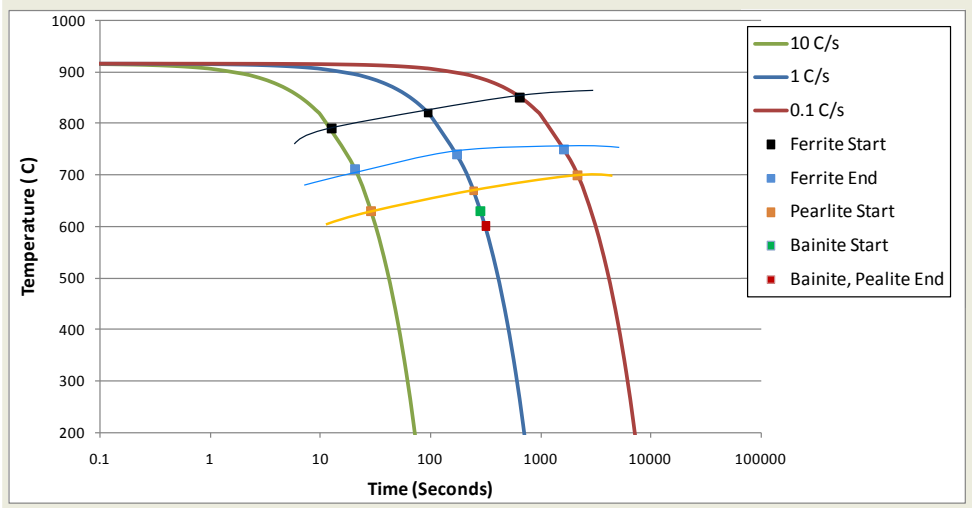


Figure 66 Continuous Cooling Diagram showing the transformation temperatures observed in the cooling experiments for 7631

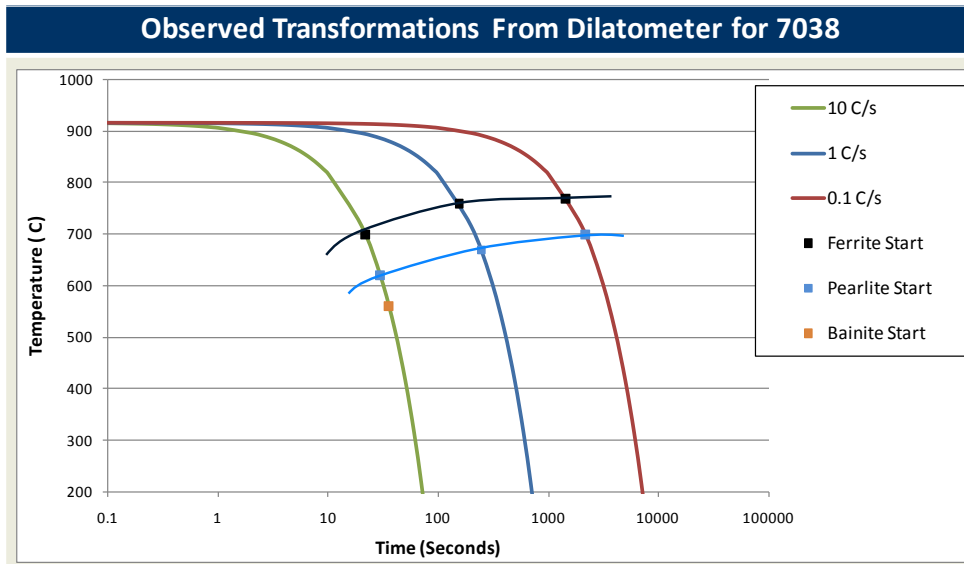


Figure 67 Continuous Cooling Diagram showing the transformation temperatures observed in the cooling experiments for 7038

The observed transformations from the dilatometer seem to confirm with some accuracy the predictions from the J-Mat Pro software.

In the dilatometer experiments hot rolled samples were reheated to the final rolling temperature provided, equalized for 15 minutes and then cooled. In this case the characteristics of the austenite in the sample can be different from the equilibrium condition that the software uses to determine the transformations during continuous cooling.

In some cases additional transformations were observed in the dilatometer. These transformations could be due to completion of ferrite or it could be that the evolution of Acicular Ferrite is having some effect on the expansion of the sample. Also, in temperature regions where multiple transformations are occurring individual transformations can be hidden within the expansion curve.

Finally, due to the nature of the dilatometer results it is necessary to observe the microstructure of the samples after the experiments in order to get an appreciation of the transformations that occurred.

6.4 TMP SIMULATIONS

Similarly to the hot-band analysis, the microstructural analysis of the samples which had undergone thermomechanical processing was used to calculate a predicted yield stress for each condition, table 18 and 19 below show the results

Table 23 Calculated yield stress predicted using extended Hall-Petch model from microstructural data analyzed from optical microscopy for 7153, 7631, and 7045

Steel	7153	7153	7631	7631	7045	7045	7045
Tcoil	650	750	550	650	550	600	650
Cooling	10	10	10	10	10	10	10
PYS (MPa)	331.1	329.78	297.41	304.02	332.86	305.99	325.77
Steel	7153	7153	7631	7631	7045	7045	7045
Tcoil	650	750	550	650	550	600	650
Cooling	30	30	30	30	30	30	30
PYS (MPa)	339.03	330.42	322.79	325.15	394.04	382.64	343.92

Table 24 Calculated yield stress predicted using extended Hall-Petch model from microstructural data analyzed from optical microscopy for 7038, “Low” denotes samples deformed at the lower finishing temperature.

Steel	7038	7038	7038 Low	7038 Low
Tcoil	550	650	550	650
Cooling	10	10	10	10
PYS (MPa)	304.68	305.45	303.54	298.5
Steel	7038	7038	7038	7038
Tcoil	650	550	650	550
Cooling	30	30	30	30
PYS (MPa)	322.92	317.33	330.55	318.14

These yield stress calculations were then compared to the values calculated for the hot-band and plotted with respect to cooling rate.

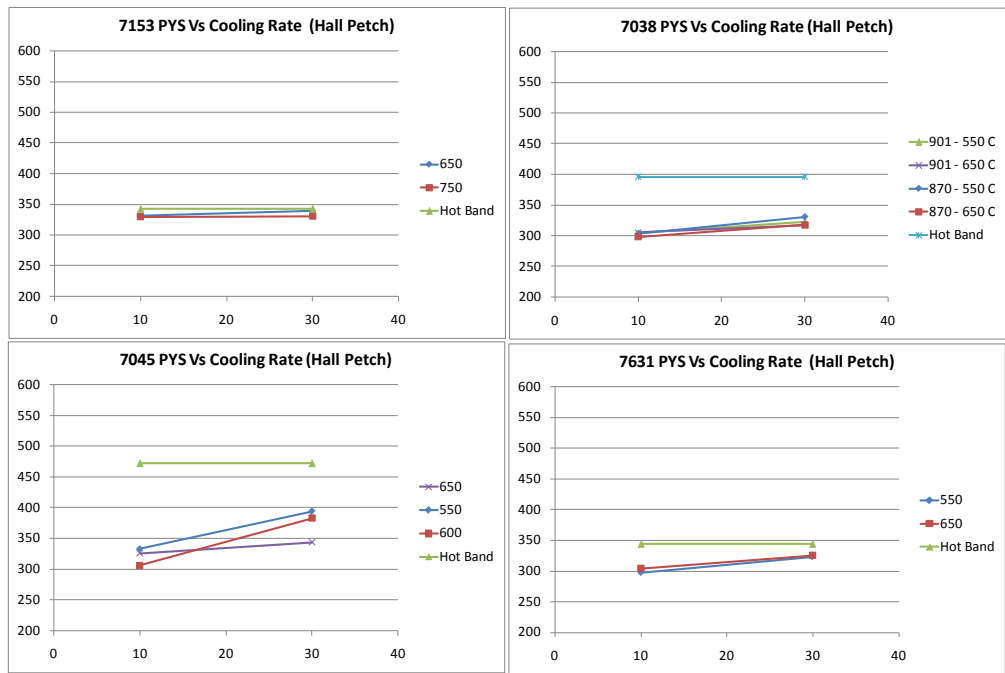


Figure 68 Comparison plots of predicted yield stress of TMP Simulation results with hot-band analysis results

The discrepancies present between some of the predicted yield stress values for the experimental samples and the values calculated for the Hot Band material are due to the resulting larger ferrite grain size inherent in most of the TMP samples. This difference in grain size is due to the sometimes significant differences in the amount of hot deformation in the provided Hot Band compared to the deformation applied in the TMP experiments. For Example, in the results for 7038 a difference of about $4\mu\text{m}$ in grain size makes the predicted yield stress change by approximately 90 MPa in the Hall-Petch relation used.

Using the data collected from the MTS compression testing machine the peak deformation stresses at each rolling temperature could be calculated from the forces recorded by the system. Figure 69 shows the average maximum true stress applied to the samples during the experiments at each rolling temperature. These results show that, at the primary four rolling temperatures, 7045, 7153, and 7038 all exhibit very similar behavior. Grade 7631, shows a much more pronounced increase in peak stress at the finishing temperature than all the other grades. Finally, at $870\text{ }^{\circ}\text{C}$, the peak stress observed in 7038 is significantly higher than that those seen at $901\text{ }^{\circ}\text{C}$ suggesting a significant change in the nature of the deformation.

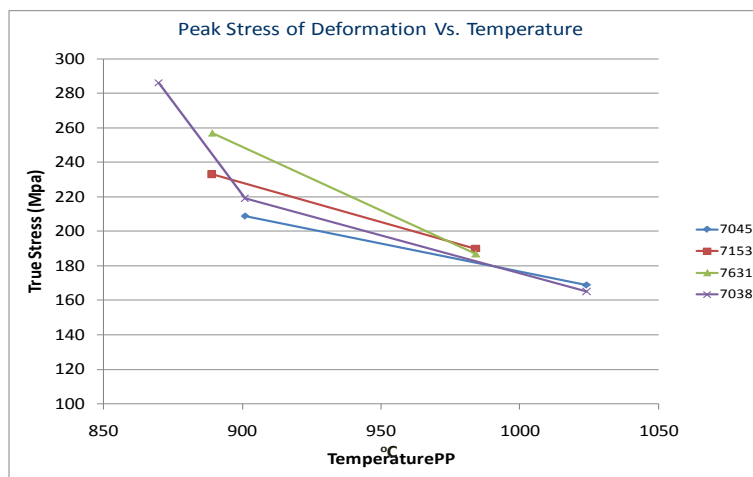


Figure 69 Plot of average peak stress at each deformation temperature for each alloy investigated.

7.0 CONCLUSIONS

The importance of well designed and implemented thermomechanical processes in order to achieve desired microstructures, strengths and toughness, in low-alloy steels, is well understood.

The microstructures in the current hot-band product has been observed and well defined, grain size and phases identified using multiple methods. Furthermore, an understanding of how the structure of these steels evolved through processing and cooling experiments.

In the continuous cooling experiments, at the highest cooling rates explored, all samples exhibited at least some low transformation product, bainitic and/or acicular ferrite formation. This observation sheds light on the importance of determining a coiling temperature that will avoid these transformations while still allowing for the high cooling rates desired from finishing to coiling.

The findings from the continuous cooling experiments directly affect how the microstructures in the TMP simulations can be interpreted. In all cases, when coiling temperatures was below the observed bainite transition in the hot-band, acicular or bainitic ferrites formed altering the microstructures, regardless of the cooling rate to coiling temperature. Looking at the effect of rolling temperature, in the 7038 samples, no significant difference was seen in the microstructure.

In the calculation for predicted yield stress from the microstructural analysis of the hot band microstructures, the predicted yield stresses were very similar to the measured yield stresses for the same steels and conditions. That is, most of the strengthening was due to solid solution and grain size refinement, very small contributions due to dislocation and precipitation strengthening were expected. The TEM results conducted on the steels containing microalloying additions supports the lack of any substantial precipitation. In the case of the predicted YS from the TMP samples, most results did not match the strengths of the hot-band. The difference was attributable to the difference in ferrite grain size. This difference in grain size has many possible factors. The most probable of which would be, the degree of deformation and number of rolling passes. The effect of austenite deformation on the formation of a fine ferrite grain is well understood in these cases. Otherwise, the microstructures formed are very similar to those in the hot band.

Finally, these results show that, with a good understanding of the cooling transition temperatures for these hot rolled materials, a processing path can be devised to provide guidelines to optimize the final microstructure of the hot band material. .

BIBLIOGRAPHY

- 1) J.H. Woodhead, S.R. Keown, "The History of Microalloyed Steels", Proceedings of an International Conference on HSLA Steels '85, Metallurgy and Applications, Beijing, China, Edited by J.M. Gray, ASM International, 1986, pp 15-28
- 2) H. de Boer, et al., "Thermomechanical Treatment of HSLA Steels Fundamentals and Realization", Proceedings of an International Conference on HSLA Steels '85, Metallurgy and Applications, Beijing, China, Edited by J.M. Gray, ASM International, 1986, pp 539-549
- 3) T. Gladman, "The Physical Metallurgy of Microalloyed Steels", Chapter 6 Thermal and Thermomechanical Cycles, The Institute of Materials, 1997, pp 231
- 4) Llewellyn, "Steels Metallurgy and Applications", Reed International, 1992, pg 75
- 5) C.M. Sellars, "Options and Constraints for the Thermomechanical Processing of Microalloyed Steels", Proceedings of an International Conference on HSLA Steels '85, Metallurgy and Applications, Beijing, China, Edited by J.M. Gray, ASM International, 1986, pp 73-82
- 6) K. Kaup, et al., Stahl und Eisen, Vol. 104, 1984, pp 1017-1024
- 7) M. Militzer, E. Howbolt, T. Meadowcroft, "Microstructural Model for the Hot Strip Rolling of High Strength Low Alloy Steels", Metallurgical and Materials Transactions A, Vol 31A, April 2000, pp 1244
- 8) L.J. Cuddy, "The Effect of Microalloy Concentration on the Recrystallization of Austenite during Hot Deformation", Proceedings of Thermomechanical Processing of MA Austenite, ed A. J. DeArdo, G. Ratz, TMS-AIME, 1982, pp129.
- 9) Tamura and C. Ouchi, Thermomechanical Processing of High Strength Low Allow Steels, 1988, pp 82.
- 10) O. Kwon, "Static Recovery and Recrystallization of Hot Deformed FCC Materials", PhD Dissertation, University of Pittsburgh, 1985
- 11) Llewellyn, "Steels, Metallurgy and Applications", Reed International, 1992, pp76
- 12) P. Peters, M. Gräf, and I. Von Hagen, AGA-EPRG-Seminar, San Francisco, 1983
- 13) K. Lorenz, and C. Düren, "Conference on Steels for Line Pipe and Pipeline Fittings", Paper 37, The Metals Society, London, 1981.
- 14) K. Sinha, "Ferrous Physical Metallurgy", Chapter 4 Nucleation in Solids, Butterworths, 1989, pp 127
- 15) T. Araki, M. Enomoto, "Microstructural Problems of Controlled Rolled and Cooled Very Low Carbon HSLA Steels" Proceedings of the 2nd International Conference on HSLA Steels: Processing, Properties, and Applications, edited by G. Tither, TMS, Beijing, China, 1990, pp 95

- 16) T. Gladman, "The Physical Metallurgy of Microalloyed Steels", Chapter 7 Properties and Applications, The Institute of Materials, 1997, pp 286
- 17) T. Gladman, "The Physical Metallurgy of Microalloyed Steels", Chapter 2 Microstructure-Property Relationship, The Institute of Materials, 1997, pp 40
- 18) G. E Dieter, "Mechanical Metallurgy", Chapter 5 Dislocation Theory, McGraw-Hill, Edited by R. Gibala, 1986, pp 181
- 19) E. O. Hall, Proceedings from the Physical Society, 1951, vol 64B, pp 747
- 20) N.J. Petch, "The Cleavage Strength of Polycrystals", Journal of the Iron and Steels Institute, vol 174, 1953, pp 25-28
- 21) K. Hulka, et al., "High Temperature Thermomechanical Processing Background and Application", Proceedings of MA 95, ISS 1995, pp 239
- 22) F. B. Pickering, Physical Metallurgy and the Design of Steels, Materials Science Series, Applied science publishers LTD, 1978, pp 65
- 23) T. Gladman, "The Physical Metallurgy of Microalloyed Steels", Chapter 2 Microstructure-Property Relationship, The Institute of Materials, 1997, pp 46
- 24) M.F. Ashby, "The Theory of the Critical Shear Stress and Work Hardening of Dispersion Hardened Crystals". Proc. of Oxide Dispersion Strengthening
- 25) E. Orowan, "The Theory of Yield without particle shear", Symposium on Internal Stresses in Metals and Alloys, edited by R.C. Gifkins, vol 1, 1982, pp 407-412
- 26) G. E Dieter, "Mechanical Metallurgy", Chapter 6 Strengthening Mechanisms, McGraw-Hill, Edited by R. Gibala, 1986, pp. 212-213
- 27) K. Sinha, "Ferrous Physical Metallurgy", Chapter 4 Nucleation in Solids, Butterworths, 1989, pp 180
- 28) R.B. Nicholson, "Effect of Second Phase Particles on the Mechanical Properties of Steel", Iron and Steel Institute, London, 1971, pp 1
- 29) G. E Dieter, "Mechanical Metallurgy", Chapter 6 Strengthening Mechanisms, McGraw-Hill, Edited by R. Gibala, 1986, pp 215
- 30) N. F. Mott and F. R. N. Nabarro, "Report on Conference on the Strength of Solids", Phys. Soc., London, 1948, pp. 1
- 31) G. E Dieter, "Mechanical Metallurgy", Chapter 6 Strengthening Mechanisms, McGraw-Hill, Edited by R. Gibala, 1986, pp. 216
- 32) L. M. Brown and R. K. Hamm, "Strengthening Methods in Crystals", Edited by A. Kelly, Elsevier, London, 1971, pp. 9
- 33) T. Gladman, "The Physical Metallurgy of Microalloyed Steels", Chapter 2 Microstructure-Property Relationship, The Institute of Materials, 1997, pp 48
- 34) T. Gladman, "Structure-Property Relationships in High-Strength MA Steels", Proceeding of MA '75, Washington, 1975, pp37
- 35) R. Herberz, H. Wiegels, Stachl Eisen, vol 101, 1981, pp 29

- 36) Electroless Nickel Plating, Metals Handbook, vol 5; Surface cleaning finishing and coating, 9th Edition, ASM, 1982, pp 219-243
- 37) Wu J., DeArdo A.J., "Diffraction Pattern Quality: A new application of EBSD to characterize microstructures"
- 38) Wu Jinghui, PhD Thesis Dissertation, Materials Science and Engineering, University of Pittsburgh, 2004
- 39) A. Ruiz-Aparicio, Master's Thesis, Materials Science and Engineering, University of Pittsburgh, 2004
- 40) M. P. Renavikar, "Small Strain Deformation Behavior of Interstitial-Free (IF) Steels", PhD Thesis Dissertation, Materials Science and Engineering , University of Pittsburgh, 2003
- 41) Rege, J., Garcia, C.I., DeArdo, A.J., "The Segregation Behavior of Phosphorus and its Role in the Cold Work Embrittlement and Annealing Behavior of Ti-stabilized Interstitial-free Steels", 39th MWSP Conference, 1998, Indianapolis, IN, ISS, pp. 149-158